

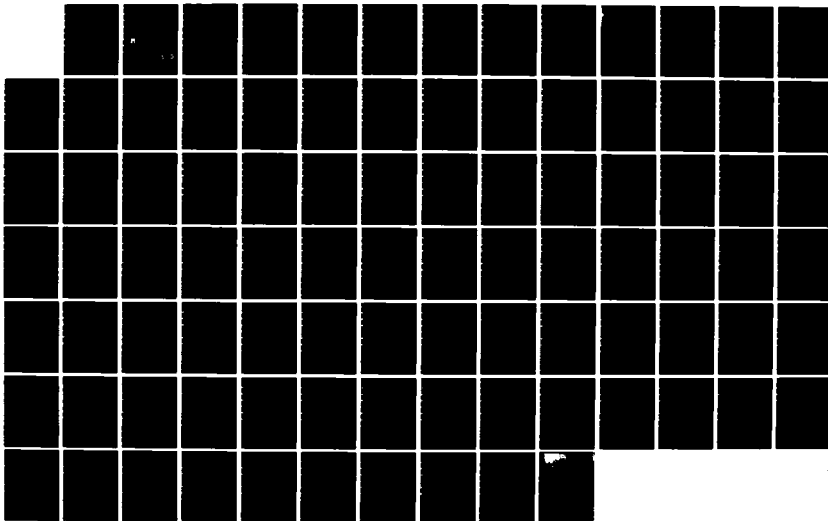
AD-A140 001

DEVELOPMENT OF A THIRD-INVARIANT PLASTICITY THEORY FOR
CONCRETE AND SOILS(U) NEW MEXICO ENGINEERING RESEARCH
INST ALBUQUERQUE H L SCHREYER FEB 84 AFWL-TR-83-119
F29601-81-C-0013 F/G 20/11

1/1

UNCLASSIFIED

NL





MICROCOPY RESOLUTION TEST CHART
NATIONAL BUREAU OF STANDARDS-1963-A

AD A140001

DEVELOPMENT OF A THIRD-INVARIANT PLASTICITY THEORY FOR CONCRETE AND SOILS

Howard L. Schreyer

University of New Mexico
New Mexico Engineering Research Institute
University Station
Albuquerque, NM 87131

February 1984

Final Report

Approved for public release; distribution unlimited.

DTIC
ELECTE
S APR 11 1984 D
B

AIR FORCE WEAPONS LABORATORY
Air Force Systems Command
Kirtland Air Force Base, NM 87117

DTIC FILE COPY

This final report was prepared by the New Mexico Engineering Research Institute, Albuquerque, New Mexico, under Contract F29601-81-C-0013, Job Order 2307Y201 with the Air Force Weapons Laboratory, Kirtland Air Force Base, New Mexico. Timothy J. Ross (NTES) was the Laboratory Project Officer-in-Charge.

When Government drawings, specifications, or other data are used for any purpose other than in connection with a definitely Government-related procurement, the United States Government incurs no responsibility or any obligation whatsoever. The fact that the Government may have formulated or in any way supplied the said drawings, specifications, or other data, is not to be regarded by implication, or otherwise in any manner construed, as licensing the holder, or any other person or corporation; or as conveying any rights or permission to manufacture, use, or sell any patented invention that may in any way be related thereto.

This report has been authored by a contractor of the United States Government. Accordingly, the United States Government retains a nonexclusive, royalty-free license to publish or reproduce the material contained herein, or allow others to do so, for the United States Government purposes.

If your address has changed, if you wish to be removed from our mailing list, or if your organization no longer employs the addressee, please notify AFWL/NTES, Kirtland AFB, NM 87117 to help us maintain a current mailing list.

This technical report has been reviewed and is approved for publication.


TIMOTHY J. ROSS
Project Officer


PAUL E. MINTO
Captain, USAF
Chief, Applications Branch

FOR THE COMMANDER


JOHN H. STORM
Colonel, USAF
Chief, Civil Engineering Research Div

DO NOT RETURN COPIES OF THIS REPORT UNLESS CONTRACTUAL OBLIGATIONS OR NOTICE ON A SPECIFIC DOCUMENT REQUIRES THAT IT BE RETURNED.

UNCLASSIFIED

SECURITY CLASSIFICATION OF THIS PAGE

AD A140 001

REPORT DOCUMENTATION PAGE

| | | | | |
|--|-------------|--|--|--|
| 1a. REPORT SECURITY CLASSIFICATION Unclassified | | | 1b. RESTRICTIVE MARKINGS | |
| 2a. SECURITY CLASSIFICATION AUTHORITY | | | 3. DISTRIBUTION/AVAILABILITY OF REPORT Approved for public release; distribution unlimited. | |
| 2b. DECLASSIFICATION/DOWNGRADING SCHEDULE | | | | |
| 4. PERFORMING ORGANIZATION REPORT NUMBER(S) | | | 5. MONITORING ORGANIZATION REPORT NUMBER(S) AFWL-TR-83-119 | |
| 6a. NAME OF PERFORMING ORGANIZATION University of New Mexico New Mexico Engrg Rsch Inst | | 6b. OFFICE SYMBOL (If applicable) | 7a. NAME OF MONITORING ORGANIZATION Air Force Weapons Laboratory | |
| 6c. ADDRESS (City, State and ZIP Code) University Station Albuquerque, NM 87131 | | | 7b. ADDRESS (City, State and ZIP Code) Kirtland Air Force Base, NM 87117 | |
| 8a. NAME OF FUNDING/SPONSORING ORGANIZATION | | 8b. OFFICE SYMBOL (If applicable) | 9. PROCUREMENT INSTRUMENT IDENTIFICATION NUMBER F29601-81-C-0013 | |
| 8c. ADDRESS (City, State and ZIP Code) | | | 10. SOURCE OF FUNDING NOS. | |
| | | | PROGRAM ELEMENT NO. 61102F | PROJECT NO. 2307 |
| | | | TASK NO. Y2 | WORK UNIT NO. 01 |
| 11. TITLE (Include Security Classification) DEVELOPMENT OF A THIRD-INVARIANT PLASTICITY THEORY FOR CONCRETE AND SOILS | | | | |
| 12. PERSONAL AUTHOR(S) Schreyer, Howard L. | | | | |
| 13a. TYPE OF REPORT Final | | 13b. TIME COVERED FROM <u>82 Oct</u> TO <u>83 Sep</u> | | 14. DATE OF REPORT (Yr., Mo., Day) 1984, February |
| 15. PAGE COUNT 92 | | | | |
| 16. SUPPLEMENTARY NOTATION | | | | |
| 17. COSATI CODES | | | 18. SUBJECT TERMS (Continue on reverse if necessary and identify by block number) | |
| FIELD 20 | GROUP 11 | SUB. GR. | Viscoplasticity Strain Rate Concrete Cracking Soils | |
| 19. ABSTRACT (Continue on reverse if necessary and identify by block number) A viscoplastic constitutive relation for frictional materials has been formulated and applied to concrete and soils. First and third invariants of both stress and strain are used instead of the more conventional second invariants employed in relations for metal plasticity. Detailed comparisons between theoretical and experimental data are made for a variety of paths involving weak concrete and sandy soils. For the soils, both static and dynamic behavior are considered. The model has been extended to incorporate cracking based on a maximum principal stress criterion. Proposed experimental and theoretical work will cover rate effects in concrete, the response of unsaturated clay, and interfaces between soil and concrete. | | | | |
| 20. DISTRIBUTION/AVAILABILITY OF ABSTRACT UNCLASSIFIED/UNLIMITED <input checked="" type="checkbox"/> SAME AS RPT. <input type="checkbox"/> DTIC USERS <input type="checkbox"/> | | | 21. ABSTRACT SECURITY CLASSIFICATION Unclassified | |
| 22a. NAME OF RESPONSIBLE INDIVIDUAL Dr Timothy J. Ross | | | 22b. TELEPHONE NUMBER (Include Area Code) (505) 844-9087 | 22c. OFFICE SYMBOL NTES |

CONTENTS

| <u>Section</u> | | <u>Page</u> |
|----------------|--|-------------|
| I | INTRODUCTION | 3 |
| II | RATE EFFECTS IN CONCRETE | 5 |
| | Existing Data | 5 |
| | Experimental Device for Determining Rate Effects in Concrete | 11 |
| III | VISCOPLASTIC CRACKING MODEL | 18 |
| IV | INTERFACE MODELING | 30 |
| V | RECOMMENDATIONS | 32 |
| | REFERENCES | 34 |
| | APPENDIXES | |
| | A. A THIRD-INVARIANT PLASTICITY THEORY FOR LOW-STRENGTH CONCRETE | 37 |
| | B. A THIRD-INVARIANT VISCOPLASTICITY THEORY FOR RATE-DEPENDENT SOILS | 65 |



| | |
|--------------------|-------------------------------------|
| Accession For | |
| NTIS GRA&I | <input checked="" type="checkbox"/> |
| DTIC TAB | <input type="checkbox"/> |
| Unannounced | <input type="checkbox"/> |
| Justification | |
| By | |
| Distribution/ | |
| Availability Codes | |
| Dist | Avail and/or Special |
| A-1 | |

ILLUSTRATIONS

| <u>Figure</u> | | <u>Page</u> |
|---------------|--|-------------|
| 1 | Pressure histories for some propellants | 14 |
| 2 | Conceptual test apparatus for tests at high strain rates | 15 |
| 3 | Behavior of cracking function, g , with application to uniaxial stress | 20 |
| 4 | Plasticity and cracking flow surfaces | 21 |
| 5 | Flow chart for viscoplastic-cracking algorithm | 25 |
| 6 | Uniaxial stress | 26 |
| 7 | Cracking failure for shear stress versus shear strain | 27 |
| 8 | Indirect shear response | 29 |

I. INTRODUCTION

The ability to predict the response of structures subjected to large, abrupt bursts of energy depends on a number of factors. These include load definition, the characteristics of the geological material in which the structure is embedded, the mechanism by which forces are transferred from the geological material to the structure, and the characteristics of the structure. The basic objective of the research project discussed in this report is to provide an improved understanding of the response of common geological and structural materials and of structure-media (concrete-soil) interfaces to abrupt loading. For this purpose, engineering constitutive models have been developed, and appropriate experimental data are being used to validate the models.

The initial formulation of a constitutive model for frictional materials involved the use of the theory of plasticity modified to incorporate first and third invariants of stress and strain instead of the more conventional second invariants. A nonassociated flow rule was applied to control dilatation. This theory is outlined in Appendix A, where detailed comparisons of the theoretical data with stress-strain data obtained in experiments on weak concrete may also be found. The experimental stress paths encompass a wide range and provide a comprehensive test for the model.

Rate effects represent an important feature that must be included if deformations resulting from abruptly applied loads are to be predicted accurately. A viscoplastic formulation, applied to sand and clayey sands, is given in Appendix B. Theoretical and experimental data are compared for both static and dynamic loads, and it is concluded that the model is a reasonable base for representing these soil materials as well as concrete.

There is a dearth of experimental data on multiaxial rate effects for concrete and geological materials. A survey of the literature (Section II) has disclosed that most data for concrete are based on uniaxial stress conditions with a limited range of strain rates. Also in Section II is a description of a conceptual experimental apparatus in which propellants will be used to provide forces with rise-times sufficiently small that multiaxial data for concrete with strain rates on the order of $1/s$ can be obtained.

The viscoplastic model (Appendix B) has been modified to include cracking. The procedure, described in Section III, consists of using a maximum normal tensile stress criterion combined with strain control of crack propagation. This method provides numerical stability together with a physically realistic model that can also be used with an interface model.

Several interesting developments with regard to the representation of interface phenomena have been reported in the literature. Some of the implications of these studies for the development of an interface model for soil and concrete are described in Section IV.

The primary focus for the continuation of this research project is summarized briefly in Section V. The effort will include the development of an experimental device for obtaining strain rate data on concrete, the development of interface modeling, and both theoretical and experimental investigations of the response of wet clay to triaxial loading.

II. RATE EFFECTS IN CONCRETE*

EXISTING DATA

Strain rates affect several of the mechanical properties of concrete. The extent to which these properties are affected is not easily determined because it depends upon the property being considered and the method used to prepare and test the concrete. In most of the literature it is reported that increasing the strain rate at which a test is conducted increases the compressive strength, the modulus of elasticity, and the energy absorption of the concrete. The sensitivity of a concrete to dynamic loads is related to the extent of the increase of these parameters

Testing concrete at high strain rates began in the early 1900s when the effect of impact driving on concrete piles became a matter of interest. Since that time interest in these effects has grown, and the tests have become increasingly sophisticated. A recent literature survey indicates this growth (Refs. 1-6), but large gaps in knowledge are also evident. Mainstone (Ref. 1) tried to bring together the available data on the sensitivity to strain rates of the stiffness and nominal compression strength of concrete. However, as he noted, his plot of the ratio of dynamic unconfined compression strength, f'_d , to static unconfined compression strength, f'_c , versus strain rate, $\dot{\epsilon}$, does not take into consideration such factors as aggregate stiffness and moisture content. Suaris and Shah (Ref. 5), on the other hand, have tabulated the results of many strain rate tests, including tension, flexure, and compression tests. These authors note that concrete is most sensitive to strain rate effects in tension and least sensitive in compression. They do not attempt to sort out the parameters that affect the sensitivity in any one mode of testing (i.e., tension, flexure, compression).

In the work discussed in Refs. 1, 4, 5, and 7, the first result obtained and verified was that as $\dot{\epsilon}$ increases, f'_d also increases. An immediate second result observed was that the amount of plastic strain decreases as strain rates increase (Ref. 7). In 1936, Jones and Richart (Ref. 8) performed some tests on concrete aged 7 days and 28 days. The fastest strain rate at which

*This section prepared by Susan M. Babcock, Research Engineer, New Mexico Engineering Research Institute, University of New Mexico, Albuquerque.

they tested was on the order of $10^{-3}/s$. Their results also showed that an increase in the rate of loading resulted in an increase in strength.

Watstein (Ref. 9) conducted a series of tests on weak concrete at strain rates of about 0.004/s, 1.5/s and 10/s, and on higher strength concrete at strain rates of about 0.003/s, 2.9/s, and 6.7/s. An hydraulic machine was used in performing the slower tests and a drophammer in the faster tests. Watstein concluded that the compressive strength, the modulus of elasticity, the strain energy absorption, and the strain at peak stress all increase with increasing strain rate.

In 1958, Evans (Ref. 10) reported on a series of tests performed in the 1930s in which a compressed-air testing device was used. He concluded that no definite increase in strength was apparent at loading speeds to failure slower than 1/20 s. At faster speeds he observed a definite increase in the crushing strength. Evans also observed that the percent of increase in crushing strength with increase in load rate was greater for the leaner mix (high water-to-cement ratio) than for the richer mix (low water-to-cement ratio) of concrete.

During 1964, Green (Ref. 3) performed some tests designed to determine a specimen's ability to absorb energy by withstanding repeated blows from an impacting pendulum (impact strength). Green concluded that for his set of specimens (1) the impact strength of Portland cement concrete increases with the compressive strength; (2) the impact strength is greater for concretes in which an angular rough aggregate is used; (3) the impact strength is slightly less for water-cured concrete than for air-cured concrete, and water-cured concrete resists cracking better but fails more quickly after the initial crack; (4) the effects of sand grading are slight; and (5) the modulus of rupture is not a good indicator of impact strength.

In 1966 Cowell (Ref. 11) performed a series of tests in which he investigated the effects of compressive strength of concrete and curing technique on strain rate effects. He obtained strain rates of from about $10^{-6}/s$ to 0.8/s. Cowell describes thoroughly his testing technique, specimen preparation, and results. He used medium- and high-strength concretes and cured specimens of both strengths in two ways (1) 26-day wet cure followed by 2 days at room

humidity and (2) 28-day wet cure followed by 21 days at room humidity. He observed that drying the concrete tended to lower the rate of increase in compressive strength at lower stress rates for both strengths of concrete. However, the effects of drying on the dynamic strength of the concrete were more pronounced in the higher strength concrete. He also noted that drying the concrete reduced the rate of increase of the secant modulus at lower stress rates but produced negligible effects at the maximum stress rate. Cowell also observed that the modulus of elasticity, the f'_c value, and Poisson's ratio (ν) increased with increasing loading rates for the stress rates he used. When he computed the ratio of f'_d to f'_c , the difference between the high-strength and medium-strength concretes was insignificant and could be estimated by a single curve in the space of f'_d/f'_c versus strain rate.

Also in 1966, Goldsmith, Polivka, and Yang (Ref. 12) published a paper in Experimental Mechanics describing an experimental program in which they had used the Hopkinson split bar technique. Discussions of this technique, which was originally used for metals, can be found in References 6, 13, and 14. The stress levels achieved by Goldsmith et al. (Ref. 12) were too low to produce significant damage. By comparing the modulus of elasticity from shocked portions of the long cylindrical specimen to the modulus from the unshocked portions, they were able to conclude that the dynamic modulus is significantly greater than the corresponding static modulus. The authors also studied the dispersion and attenuation of the waves propagating through the specimen. From this study they ascertained that the longitudinal waves propagated without dispersion and with little attenuation.

In 1967 Atchley and Furr (Ref. 7) performed some very slow (virtually static) tests and some drophammer tests on concrete. The authors concluded that concrete can absorb only a limited amount of energy, after which point failure will occur. However, they found it difficult to determine the cause of the initial failure. They computed values of f'_d/f'_c for their data and compared these results with data from Cowell (Ref. 11) and Watstein (Ref. 9). In the space of f'_d/f'_c versus $\dot{\epsilon}$, both Cowell's and Watstein's data formed concave upward curves; Atchley's and Furr's data formed concave downward curves. Atchley and Furr tentatively attributed the discrepancy to a difference in

strain gage locations. Cowell and Watstein had both used surface strain gages; Atchley and Furr had used internal strain gages. However, other differences among these three research efforts may have also contributed to the differing characteristics of the curves. Among these factors were differences in curing techniques, concrete age at test time, and type of coarse aggregate used. Atchley and Furr did concur with previous researchers that concrete strength increases with increasing strain rate but seems to approach asymptotically some undetermined limit within the range of strain rates measured.

In the 1970s and early 1980s, several papers were published in which parametric studies at high strain rates were discussed (Refs. 2, 4, and 15-19). The parameters studied included cement/water ratio (Refs. 8 and 16), age (Refs. 2 and 16), cement content (Refs. 8 and 16), aggregate stiffness (Refs. 16-18), coarse/fine aggregate ratio (Ref. 16), curing conditions (Refs. 2, 4, and 15), and compressive strength (Ref. 4). According to Hughes and Gregory (Ref. 16) and Hughes and Watson (Ref. 18), the dynamic strength of concrete increases slightly more at a high water/cement ratio than at lower ratios. The effect of the cement volume fraction on the dynamic-strength/static-strength ratio appears to have been insignificant in these two studies, and the authors also report that variations in type of coarse aggregate used had insignificant effects on the dynamic strength of the concrete. In one case the aggregates were limestone and gravel (Ref. 8) and in the other case, limestone and granite (Ref. 16). Sparks and Menzies (Ref. 17), on the other hand, concluded that the "sensitivity of the static strength to the rate of loading appears to be related to the stiffness of the aggregate." Their work showed that stiff aggregates such as limestone provided less increase in strength with increased load rate than did less stiff aggregates such as granite. The least stiff aggregate they tested gave the greatest increase in strength with increasing load rate.

The coarse-to-fine aggregate ratio results are plotted in Reference 16. The plot indicates that the reduction in strength effected by the lower water/cement ratio was not as great when a larger amount of fine aggregate was used. The effects of the age of the concrete on the dynamic strength, as reported by Hughes and Gregory (Ref. 16), were inconsistent. Conversely, Kaplan (Ref. 2) observed that as the age of the concrete increased from 2 days

to 29 days, the rate of increase of the dynamic strength with increasing load rate was more linear at load rates from 0.001 to 100 N/mm²s. The data for the newer concrete tended to have a definite concave upward curve in the space of compressive strength versus rate of loading.

The curing condition used for the concrete has been observed to have a significant effect on the sensitivity of the concrete to high strain rates (Refs. 2 and 4). Dhir and Sangha (Ref. 4) compared data found in the literature (Refs. 8, 9, and 10) as well as data they had obtained. They concluded that as the length of the air-cure period is increased, the effect of strain rate diminishes. This finding is supported by Kaplan's observations (Ref. 2) that moist specimens were significantly more sensitive to increasing strain rates than were drier specimens. Spooner (Ref. 15) tested for sensitivity of strain rate to cure method for relatively low strain rates (3.8×10^{-7} /s and 5.0×10^{-5} /s). His finding that air cure decreases the limit stress more than does water cure agrees with the results presented in References 2 and 4. He also noted that strain at the maximum stress does not differ significantly on the two curves. Kaplan (Ref. 2) suggests that the enhanced dynamic strength of moist concrete, as compared to dry concrete, is due to the hydrostatic pressure in the pores, which delays microcracking and allows a higher compressive strength to develop.

Dhir and Sangha (Ref. 4) also studied the effect of the nominal strength of the concrete on the sensitivity of the concrete to increasing strain rates, as reported in the literature. They found conflicting data. They reported that some data, such as those obtained by Watstein (Ref. 9), showed a slight increase in sensitivity to higher strain rates when the nominal strength of the concrete was increased. This reported trend in Watstein's data does not seem to be confirmed by Watstein's own report. Other data (Refs. 8 and 10) indicated that sensitivity to strain rate is independent of concrete strength. On the basis of their own experience with sandstones ("natural" concretes) at relatively low rates of loading, Dhir and Sangha (Ref. 4) concluded that the percent increase in the dynamic strength of higher strength concretes is greater than that of low-strength concretes. Some discrepancies regarding the enhancement of dynamic concrete strength and its association with static concrete strength are evident in the findings of various authors. The

conclusions of Dhir and Sangha, for example, differ from the conclusions Mainstone (Ref. 1) reached after reviewing several papers (among others, Refs. 8, 9, 10, 16, and 17).

For the data discussed so far, the compression tests were uniaxial stress tests. Only two types of multiaxial tests were described in the literature. Biaxial testing with a very large hydropneumatic biaxial device and a device based on the Hopkinson bar has been accomplished on metals and has been proposed for concrete (Ref. 19). The other type of multiaxial test was performed by Takeda, Tachikawa, and Fijimoto (Ref. 20). These workers conducted some triaxial tests in which the confining pressure was applied statically and the axial stress was applied at a high strain rate. They drew no conclusions regarding multiaxial rate effects.

On the basis of the data obtained, the following conclusions can be drawn:

1. As the loading or strain rate increases, f'_d increases. There is some dispute about whether the ratio of f'_d/f'_c continues in an accelerating fashion when plotted against $\dot{\epsilon}$, as concluded in Refs. 4, 9, 10, and 11 among others, or levels off as $\dot{\epsilon}$ becomes very large (Ref. 7).

2. As the strain rate increases, the amount of plastic strain decreases. A related factor is the increase found in the secant modulus and the late-time tangent modulus. The initial tangent modulus apparently remains constant over the spectrum of strain rates.

3. The type of coarse aggregate used in the concrete has a major effect upon the sensitivity of the concrete to strain rate effects. The stiffer aggregates give less sensitivity than do the less stiff aggregates.

4. The moisture content of the concrete has a significant influence on the sensitivity of the concrete to strain rate effects. Concretes with high moisture contents are more sensitive than are drier concretes.

A data base is beginning to emerge for uniaxial compression tests on concrete at a variety of strain rates. Even though some of the data conflict, one-dimensional constitutive models can be developed by attempting to match the most relevant data set for a particular application. To expand to more

dimensions, assumptions and engineering judgment must be used because there are virtually no data for multiaxial strain rate effects. Bazant and Oh (Ref. 21) commented that three-dimensional effects such as inelastic compaction, shear enhanced compaction, and dilatation probably are not significant at high strain rates and can be neglected in the development of models. On the other hand, these three-dimensional effects have only recently been recognized for their importance in the static three-dimensional modeling of concrete. Therefore, to determine the importance of three-dimensional effects at high strain rates, multiaxial high-strain-rate tests must be performed. From the uniaxial stress tests, significant parameters are becoming apparent. These same parameters may prove to be important in the multiaxial tests discussed in the next subsection. On the basis of the papers reviewed, it is clear that the parameters and techniques used in the proposed multiaxial tests must be well defined and documented. This matter will become particularly important as later researchers try to incorporate the test data into a unified data base.

EXPERIMENTAL DEVICE FOR DETERMINING RATE EFFECTS IN CONCRETE

Data from multiaxial stress tests at high rates of strain are virtually nonexistent. Because of the lack of multiaxial data, any attempt to model the multiaxial behavior of concrete requires that assumptions be made. The effects of high strain rates on the three-dimensional behavior of concrete are unknown. To fill this void, a relatively simple and inexpensive testing procedure is proposed.

Concrete is used in a number of applications that expose the concrete to high strain rates. Airblast and ground motion loadings from explosive shocks are two examples of such exposure. Other examples include the impact driving of concrete piles, the accidental dropping of concrete structural members during handling, high winds, earthquakes, and sudden increases in pressure in concrete vessels. Most of these events can involve strain rates ranging from virtually static ($10^{-6}/s$) to as high as $10^6/s$. It has been shown that at strain rates of less than about $0.1/s$, insignificant or confusing and unconfirmable results are obtained (Ref. 1). On the other hand, for the large majority of strain environments that protective structures are expected to survive, particularly airblast, ground shock, wind, and earthquake, the strain

rates are less than 10/s. For these reasons, the strain rates sought in an experimental program should fall between 0.1/s and 10/s.

The rise-time to peak stress can be determined for a particular concrete once $\dot{\epsilon}$ is given. The stress rate, $\dot{\sigma}$, can be approximated for uniaxial stress by

$$\dot{\sigma} \approx E\dot{\epsilon}$$

where E is the modulus of elasticity. To find the approximate rise-time for a given strain rate, the stress rate is calculated, and the time required to reach f'_c can then be determined. For example, at a strain rate of 10/s and a compressive strength of 27.6 MPa (an average-strength concrete), E is calculated to be 2.5×10^4 MPa (Ref. 22), and $\dot{\sigma}$ is 25×10^4 MPa/s. Therefore, the rise-time is $26.7 \text{ MPa} / 25 \times 10^4 \text{ MPa-s}$, or approximately 0.1 ms.

The size of the concrete test specimen is constrained by two factors. The minimum size is limited by the nonhomogeneous nature of concrete. The specimen must be large enough to ensure that the nonhomogeneities in the concrete can be neglected. To obtain this homogenization, it is generally assumed that the specimen must be at least 10 times the size of the largest aggregate in the mix. Usually, a 3/8-in coarse aggregate is used, which means that the minimum specimen size is about 100 mm. Conversely, to eliminate the effects of inertia associated with the passage of waves, the maximum specimen size must be limited in order to minimize the transit time of the wave (or to maximize the number of wave reflections). If the number of wave reflections is not sufficiently large during loading, the strain across the specimen cannot be considered uniform and the equations of motion will have to be solved and constitutive information backed out indirectly. For a large number of reflections the response can be considered homogeneous and quasi-static. The transit time is calculated from the wave speed in concrete (about 3000 m/s) and from the specimen size. The minimum specimen size of 100 mm gives a transit time of about 33 μs . With a strain rate of 10/s, the rise-time is calculated to be 0.1 ms, and three reflections will occur before a stress of f'_c is reached. A strain rate of 1.0/s requires a rise-time of 10 ms, and 300

reflections will occur before f'_c is reached. Three hundred reflections are more than enough to ensure that the effects of inertia will not significantly affect the results; three reflections probably are not enough. The minimum number of reflections will have to be determined analytically by a comparison of the dynamic solution with the static solution. As an initial estimate, at least 25 to 50 reflections will be required, which would limit the highest quasi-static $\dot{\epsilon}$ to about 1/s. If the specimen is loaded from both sides, which effectively reduces the transit time by one-half, a quasi-static $\dot{\epsilon}$ of about 2/s could be obtained. Higher strain rates can be obtained, but the calculation of stress may involve the use of the equation of motion.

Figure 1 shows typical examples of pressure histories for some propellants. It is evident that rise-times of less than 10 ms can be achieved; thus, these materials could be used to obtain the required loading rates. Gunpowder, another readily available propellant, can produce a faster rise-time as well as higher pressures than those shown in Figure 1 and thus represents an option to be considered.

The proposed testing apparatus, shown in Figure 2a, is basically a thick-walled steel tube bent into an oval. The two pressure chambers are shown in Figure 2b. The high-pressure chamber maintains a pressure at which the propellant will burn properly; the low-pressure chamber provides the forcing function for the specimen. Variations in the orifice configuration of the steel plate separating the high- and low-pressure chambers can be used to tailor the waveform. Larger holes in the plate will produce a faster rise-time in the low-pressure chamber, and smaller holes will produce a slower rise-time. The exact configurations that produce the desired strain rates in the concrete must be determined by experimentation. When strain gages are mounted on a platen, the platen becomes a load cell that can be used with strain gages installed on the concrete specimens to obtain stress-strain curves.

The concrete specimen can be cylindrical for the initial feasibility experiments. Uniaxial stress tests are sufficient for this preliminary phase. When cylindrical specimens are used, the design of the steel platen is considerably simplified because the platens can be simple cylinders also. Once

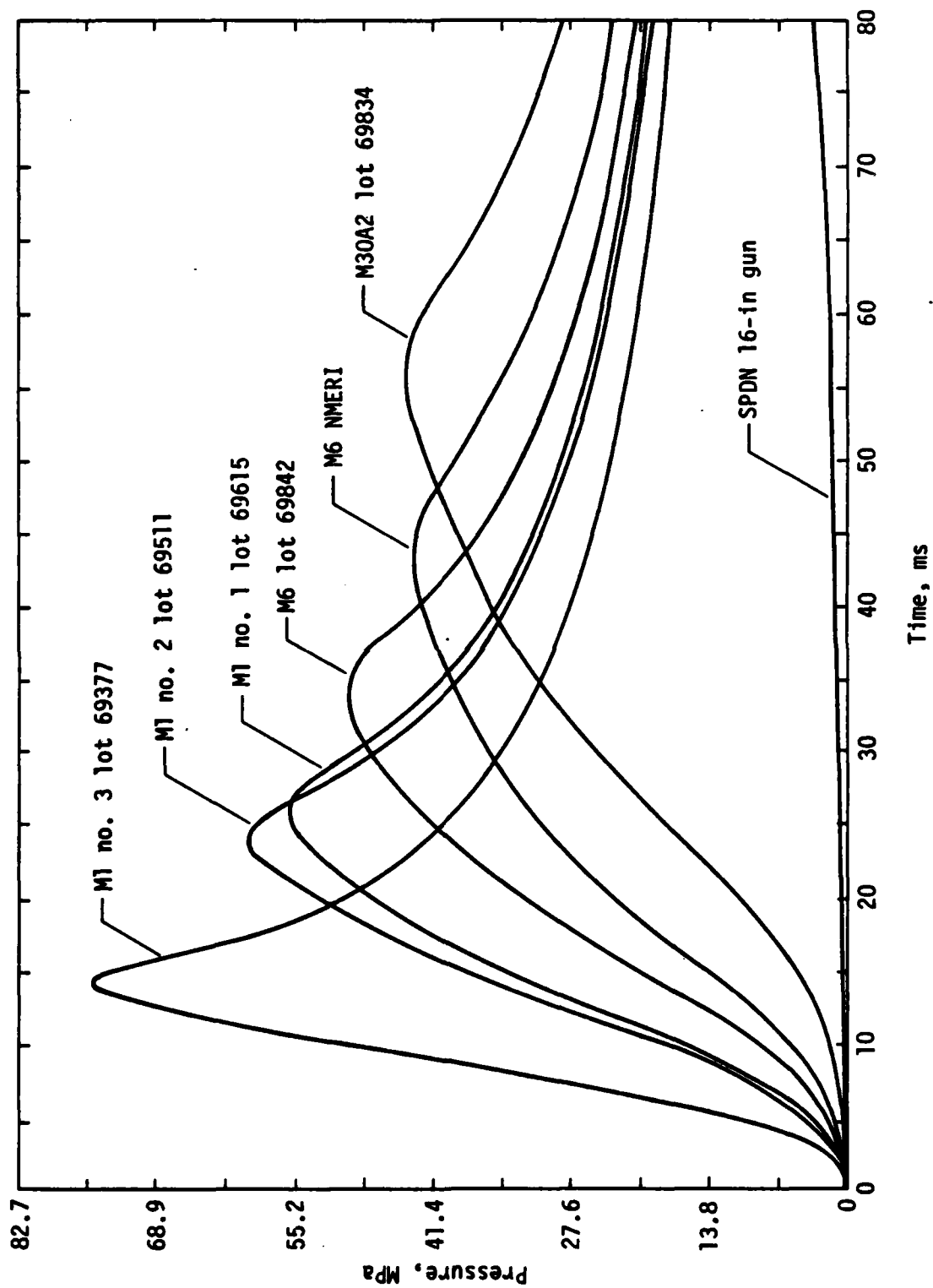
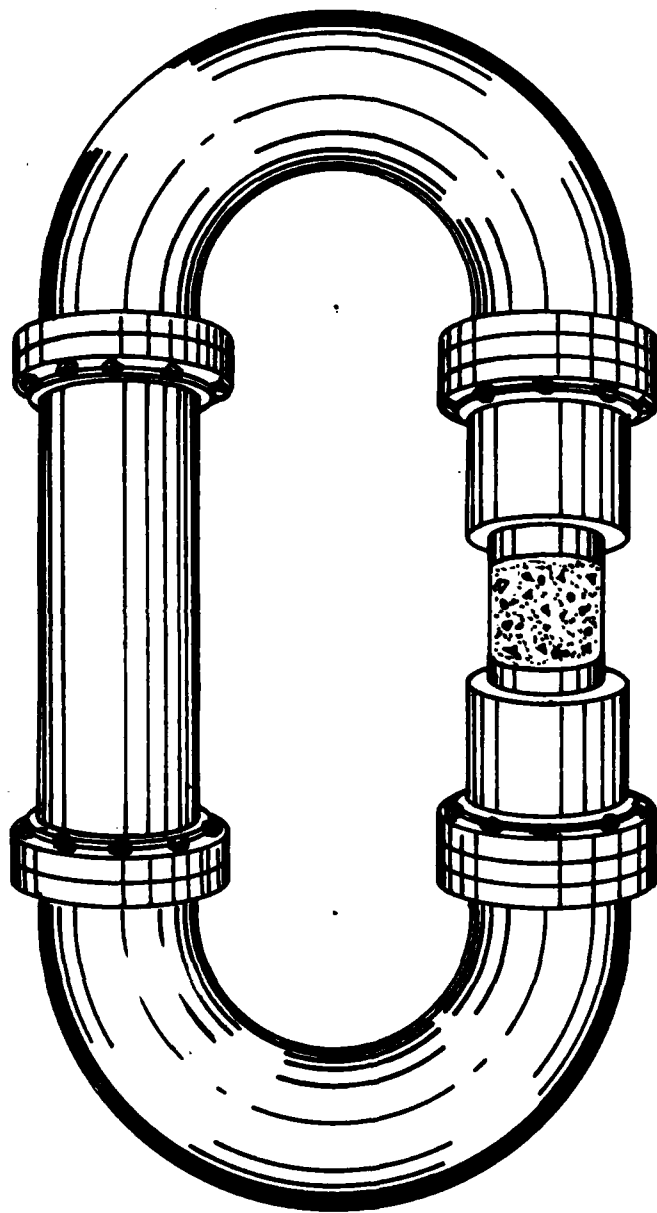
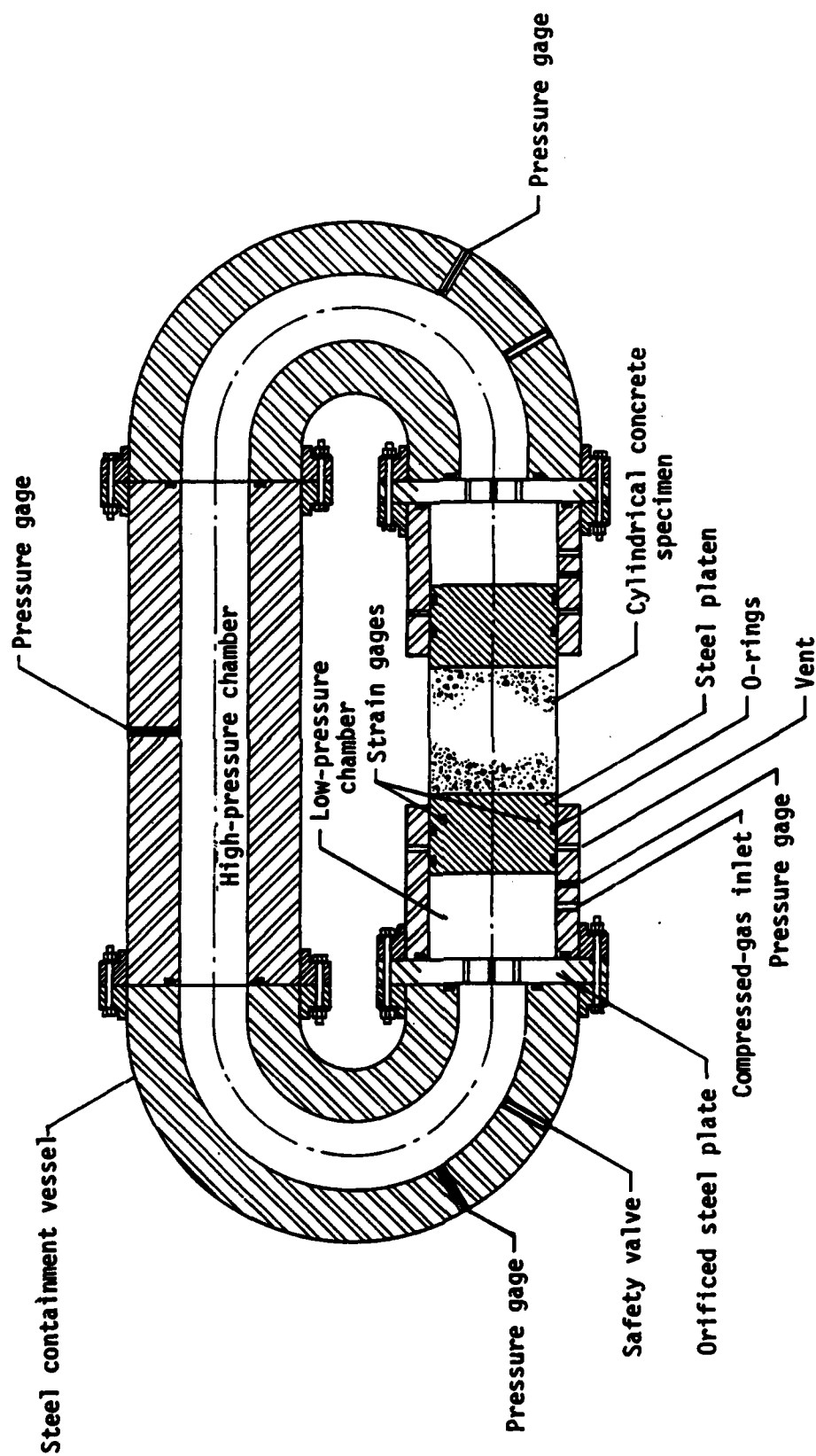


Figure 1. Pressure histories for some propellants.



(a) General schematic.

Figure 2. Conceptual test apparatus for tests at high strain rates.



(b) Cross section.

Figure 2. Concluded.

the apparatus and the technique have been thoroughly tested, modified as necessary, and verified, more complex stress path tests and specimen shapes can be used. Cubical specimens can be used to advantage in multiaxial stress path tests because they allow a variety of stress paths. However, a cubical specimen requires a more complicated platen design: the face of the platen must be square, and the back must be circular to enable the platen to fit inside the pressure vessel.

With the proposed testing apparatus, a great variety of stress-defined path tests could be conducted. Conventional static uniaxial stress tests can be performed if a powerful enough air compressor can be found or if very slow burning propellants are used. Triaxial tests on a cylindrical specimen can be undertaken by pressurization of the lateral surface. Biaxial static or quasi-static tests can be performed on cubical specimens if two sets of apparatuses on orthogonal axes are used. In any of these modes, strain rate tests, at various strain rates, can be accomplished by using the appropriate amounts of propellant.

III. VISCOPLASTIC CRACKING MODEL

An important part of the research effort has been the formulation and development of an algorithm that combines cracking with the conventional plasticity algorithm for frictional materials. Almost any problem of engineering significance involves zones in which one or more principal components of the stress tensor go into tension. To ignore this feature or to use a simple mean-pressure cutoff provides misleading results. On the other hand, a detailed cracking algorithm is often more accurate than warranted by the needs of the analyst, and the result is an inefficient numerical procedure. The approach described here is an attempt to provide an approximation procedure that is both fast and reasonably accurate.

Tensile stresses appear in a variety of engineering problems. For those involving frictional materials rather than metals, the situation is more complicated because frictional materials behave differently in tension and in compression. Consequently, both the theory and the computational algorithm must be adjusted to reflect actual tensile behavior. This behavior is partially understood for uniaxial tensile stress only; for more complex states of stress, considerable engineering judgment must be used. Because of this uncertainty, theoretical and numerical algorithms should be kept as simple as possible so that the highest possible efficiency and also a level of accuracy consistent with the available experimental data can be achieved. In the procedure proposed here, the plasticity algorithm used for conventional plasticity in the compressive regime is used to simulate cracking.

Tensile cut-off behavior is often based on mean pressure, but numerous results indicate that this approximation is not adequate. The reason is that one stress component can be large in tension, but as long as the other principal stresses are sufficiently large in compression, such a model does not predict cracking. Here, it is assumed that physical behavior is better represented by the monitoring of individual components.

Suppose one component of the stress tensor goes into tension. It is assumed that the response is elastic up to the cracking stress, σ_c , and that cracking does not occur abruptly. Instead, cracking occurs gradually as a function of tensile strain. The difference between total strain and elastic strain is called the cracking strain (e^C). The cracking stress is also

assumed to reduce linearly with total tensile strain. The rate of reduction is large but finite, and this finiteness helps to stabilize the numerical algorithm. Also, the cracking strain limit, e_L^C , is a parameter that can be used to relate energy dissipation to finite-element size so that results for crack propagation can be made invariant with respect to the finite-element mesh.

To accommodate this feature within a plasticity algorithm, a cracking potential function is defined:

$$\phi_C = \sigma - g(e^C) \quad (1)$$

where σ (positive in tension) denotes the stress component of interest, g the cracking function, and e^C the corresponding cracking strain component. Similar to the sign convention for ϕ used with plasticity, the cracking algorithm is not activated if $\phi_C < 0$ or $\sigma < g$. Also, $\phi_C > 0$ is not allowed, and cracking is considered to be occurring if $\phi_C = 0$ or $\sigma = g$. The cracking function, g , reduces linearly from σ_0^C to zero as the cracking strain increases to e_L^C , which denotes a complete fracture. For $e^C > e_L^C$, g is zero.

Also in analogy to conventional plasticity, the total tensile strain is taken to be the sum of the cracking strain and the elastic strain:

$$e = e^C + e^e \quad (2)$$

and the stress is related to the elastic strain through the conventional elasticity constitutive relations. If a stress reversal occurs, the crack closes and the conventional relations for plasticity are used in compression. However, a second reversal results in a limited tensile stress component based on the accumulated cracking strain (Fig. 3).

To indicate how the procedure works in higher dimensions, consider a case of plane stress (principal stresses) with flow surfaces as shown in Figure 4. The solid line labeled $\phi = 0$ represents a conventional plasticity flow surface, while $\phi_1 = 0$ and $\phi_2 = 0$ represent cracking flow surfaces for stress

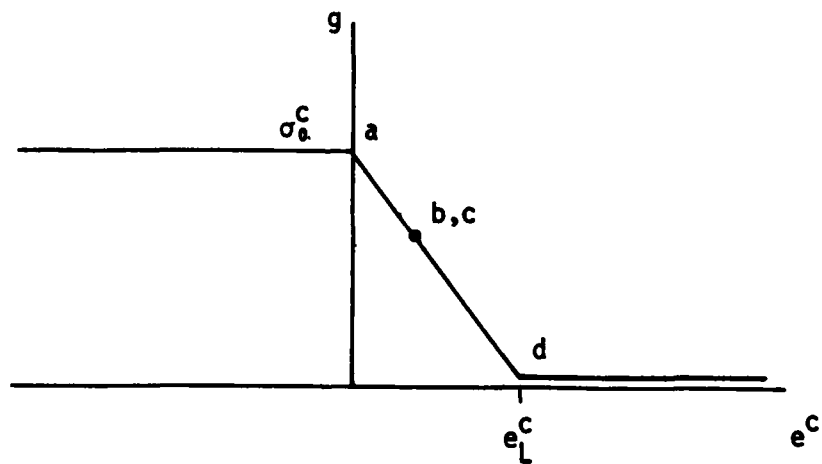
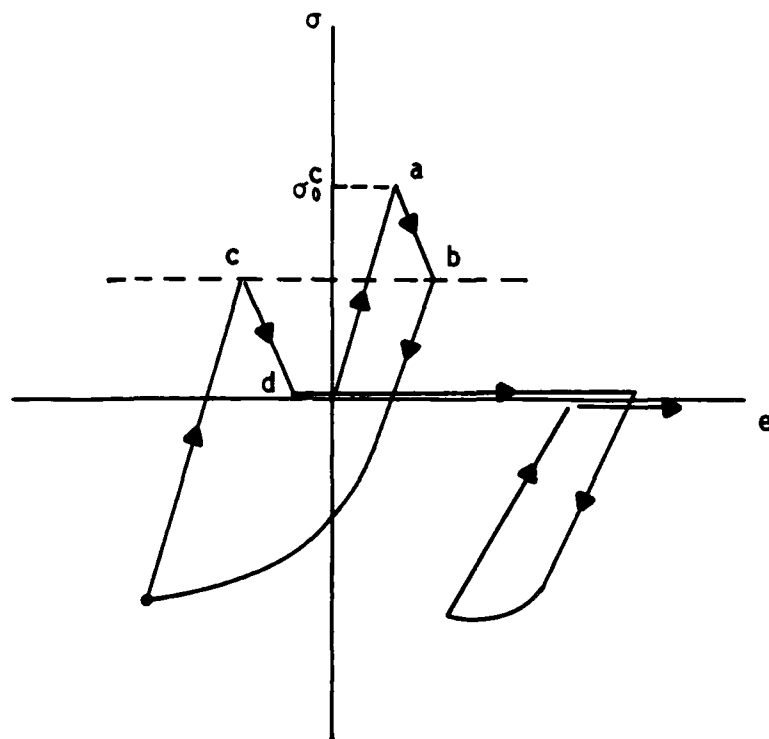


Figure 3. Behavior of cracking function, g , with application to uniaxial stress.

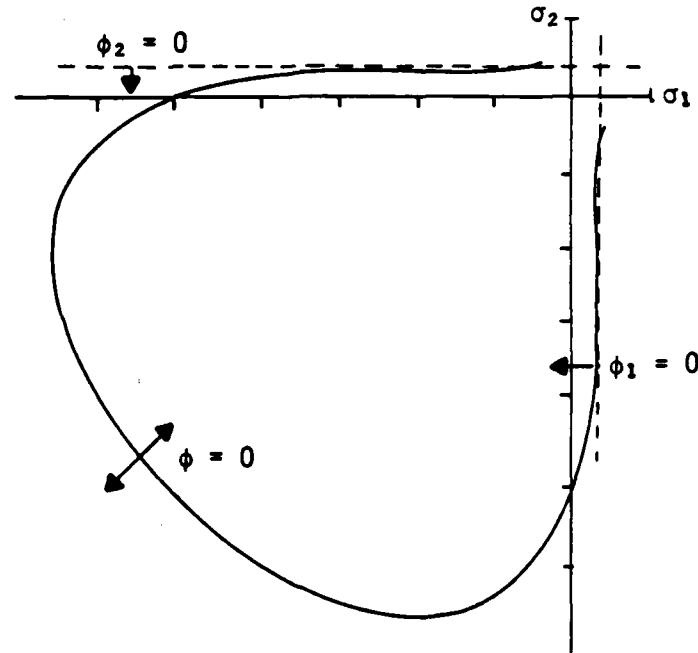


Figure 4. Plasticity and cracking flow surfaces.

components σ_1 and σ_2 , respectively. If de_1^i and de_2^i (positive in tension) denote normal components of inelastic strain, then corresponding components of cracking strain are defined as follows:

$$\begin{aligned} de_1^C &= de_1^i & \text{if } de_1^i > 0 & & de_2^C &= de_2^i & \text{if } de_2^i > 0 \\ &= 0 & \text{if } de_1^i < 0 & & &= 0 & \text{if } de_2^i < 0 \end{aligned} \quad (3)$$

$$e_1^C = \int de_1^C \quad e_2^C = \int de_2^C \quad (4)$$

That is, the cracking strains are considered to be the monotonic accumulation of inelastic tensile increments. The cracking strains that are obtained directly from surfaces $\phi_1 = 0$ and $\phi_2 = 0$ are not assumed to affect the plasticity region. However, positive inelastic strains (dilatation) from the plasticity surface are assumed to affect the cracking surface. A detailed investigation of experimental data will be required to determine whether these assumptions are reasonable.

On the flow surfaces $\phi_1 = 0$ and $\phi_2 = 0$, an associated flow rule is used. For example, consider the surface limiting the first component of stress:

$$\phi_1 = \sigma_1 - g_1(e_1^c) \quad (5)$$

where g_1 is a function similar to the function g shown in Figure 3. The inelastic strain increments are then given by the conventional flow rule of plasticity:

$$de_1^i = d\lambda \frac{\partial \phi_1}{\partial \sigma_1} = d\lambda \quad (6)$$

$$de_2^i = d\lambda \frac{\partial \phi_1}{\partial \sigma_2} = 0 \quad (7)$$

The magnitude of the scalar parameter, $d\lambda$, is determined by enforcing the consistency condition $\phi_1 = 0$. Thus, for excursions in stress dominated by a tensile component, σ_1 , the inelastic strain component de_1^i accumulates, but e_2^i does not change because $de_2^i = 0$. As cracking continues, σ_1 decreases to zero, representing a complete crack, and σ_2 adjusts automatically according to the stress-strain relations of elasticity.

It is assumed that the cracking strength in the second coordinate direction is not affected by cracking in the first coordinate direction (cracks perpendicular to the first coordinate direction) and the reverse. This assumption is carried even farther for the case of shear where shear failure is assumed to be independent of tensile cracking, i.e., there is no interaction between normal and shear strains. Although it is known that the assumption cannot be completely valid, it should be reasonable for materials such as concrete because of aggregate interlock. There is some interaction, but only if the tensile strains become large. The cracking function ϕ_{12} used for shear is similar to that used for a normal component; thus, the corresponding cracking function (potential function) and flow relation are

$$\phi_{12} = |\sigma_{12}| - g_{12}(|e_{12}^c|) \quad (8)$$

and

$$\begin{aligned} de_{12}^c &= d\lambda \frac{\partial \phi_{12}}{\partial \sigma_{12}} \\ &= d\lambda \text{sign}(\sigma_{12}) \end{aligned} \quad (9)$$

where g_{12} is also similar to g .

The problem with this formulation is that cracking strains can accumulate for states with a large mean pressure, which is not realistic. A way to circumvent this problem is to scale the cracking strain increments with mean pressure, just as the inelastic strain invariant is scaled with mean pressure.

At the end of a problem, the accumulated cracking strain components are available at each node or element according to the numerical formulation. These tensor components can be expressed in terms of principal values, which are associated with principal directions. If a principal value is positive, an appropriate interpretation would be that a crack has formed with a normal in the corresponding principal direction. For example, if only a shear cracking strain is developed, this could correspond to a crack oriented at 45 deg to the given coordinate axes.

For the numerical algorithm, strain increments are assumed given and a trial state of stress based on an elastic step is obtained. The cracking functions are checked first, and if any of them has a value greater than zero, the material is allowed to crack until a redistribution of stress and strain reduces the value to zero. The plasticity function is then checked; if it has a value greater than zero, plastic deformation is allowed to occur until this value is reduced to zero. The process is repeated iteratively until all functions are ≤ 0 . The algorithm is then exited.

This process of satisfying two or more flow functions simultaneously is actually an application of the condition that at a corner of a yield surface that does not have a continuous slope, the inelastic strain increment must fall between the normals of the respective yield functions at the intersection point. All equations are supposed to be satisfied simultaneously, but given the nature of the assumptions on cracking, the iterative procedure should not introduce unacceptable errors.

A flow chart of the algorithm is given in Figure 5. The flow functions are defined as follows for states of stress as general as plane stress and plane strain:

$$\phi_1 = L - \gamma P - \sigma_s \quad (\text{plasticity})$$

$$\phi_2 = \sigma_1 - g_1(e_1^C) \quad (\text{cracking 1-direction})$$

$$\phi_3 = \sigma_2 - g_2(e_2^C) \quad (\text{cracking 2-direction})$$

$$\phi_4 = \sigma_3 - g_3(e_3^C) \quad (\text{cracking 3-direction})$$

$$\phi_5 = |\sigma_{12}| - g_{12}(e_3^C) \quad (\text{cracking 1-2 shear})$$

in which the terms in ϕ_1 are defined in Appendix A; σ_1 , σ_2 , and σ_3 are normal components of stress; σ_{12} is a shear component; and the functions g_1 , g_2 , g_3 , and g_{12} are similar to g .

A few elementary path tests were used to check the basic algorithm in order to ensure that essential response characteristics were being reproduced. The paths and results are described as follows.

Path 1, uniaxial stress (Figs. 6a and 6b)

- a. Load σ_{11} into compression.
- b. Release and load into tension.
- c. Continue to impose tensile strain.
- d. Load into compression.
- e. Superimpose increment of tensile strain (material can no longer sustain any tensile stress).

Path 2, pure shear (Fig. 7)

A shear strain is applied monotonically, which causes the shear stress to build to the cracking level, decrease to zero, and remain there.

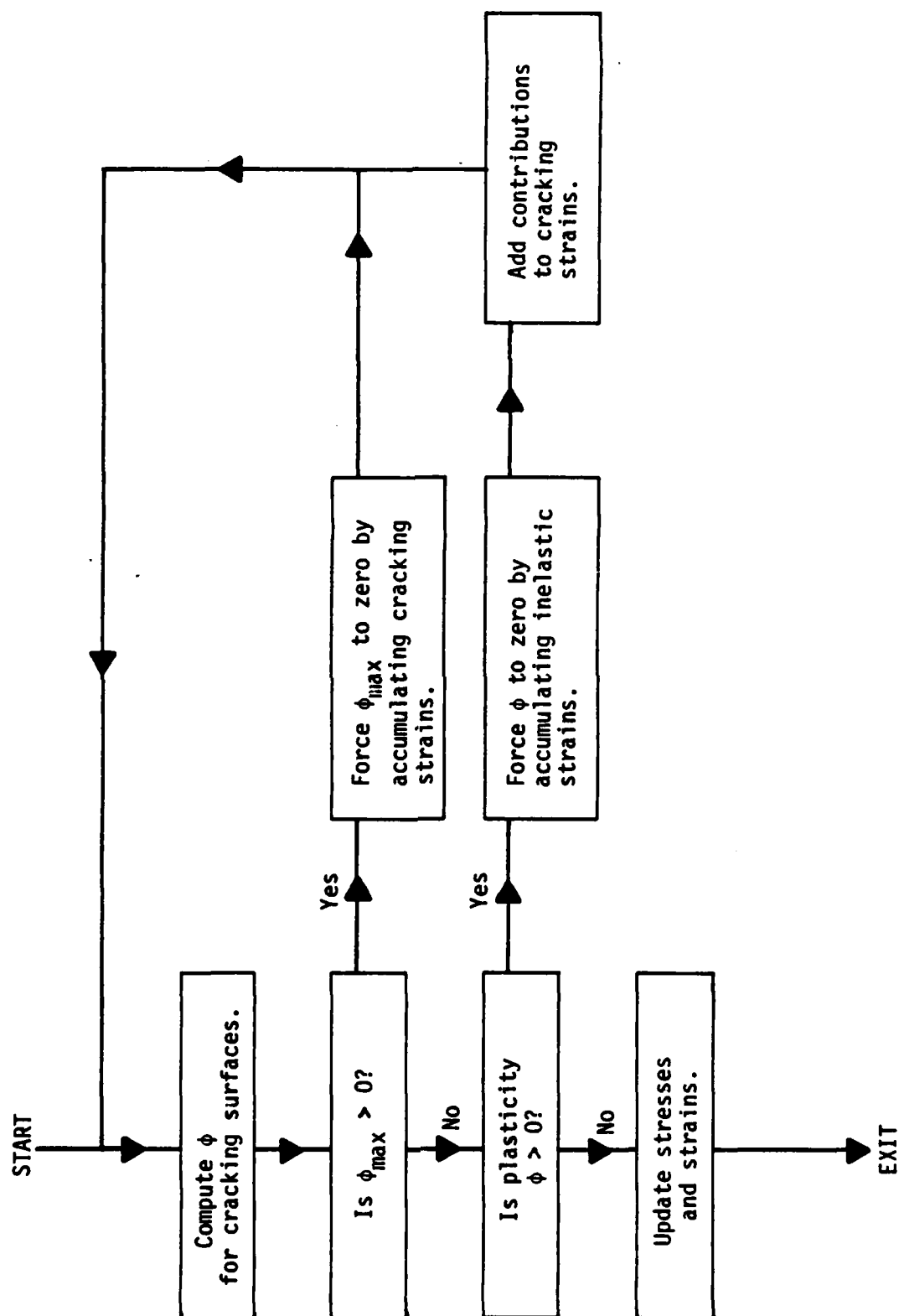
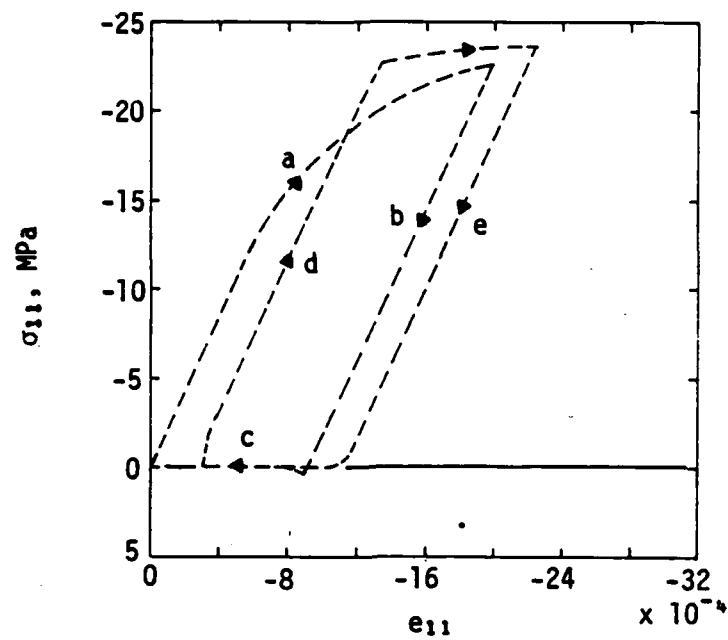
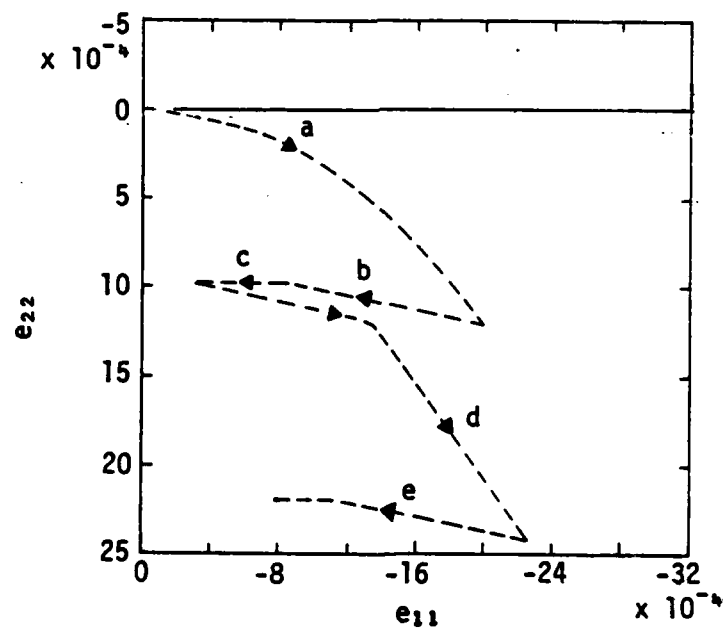


Figure 5. Flow chart for viscoplastic-cracking algorithm.



(a) Longitudinal stress versus strain.



(b) Lateral strain versus longitudinal strain.

Figure 6. Uniaxial stress.

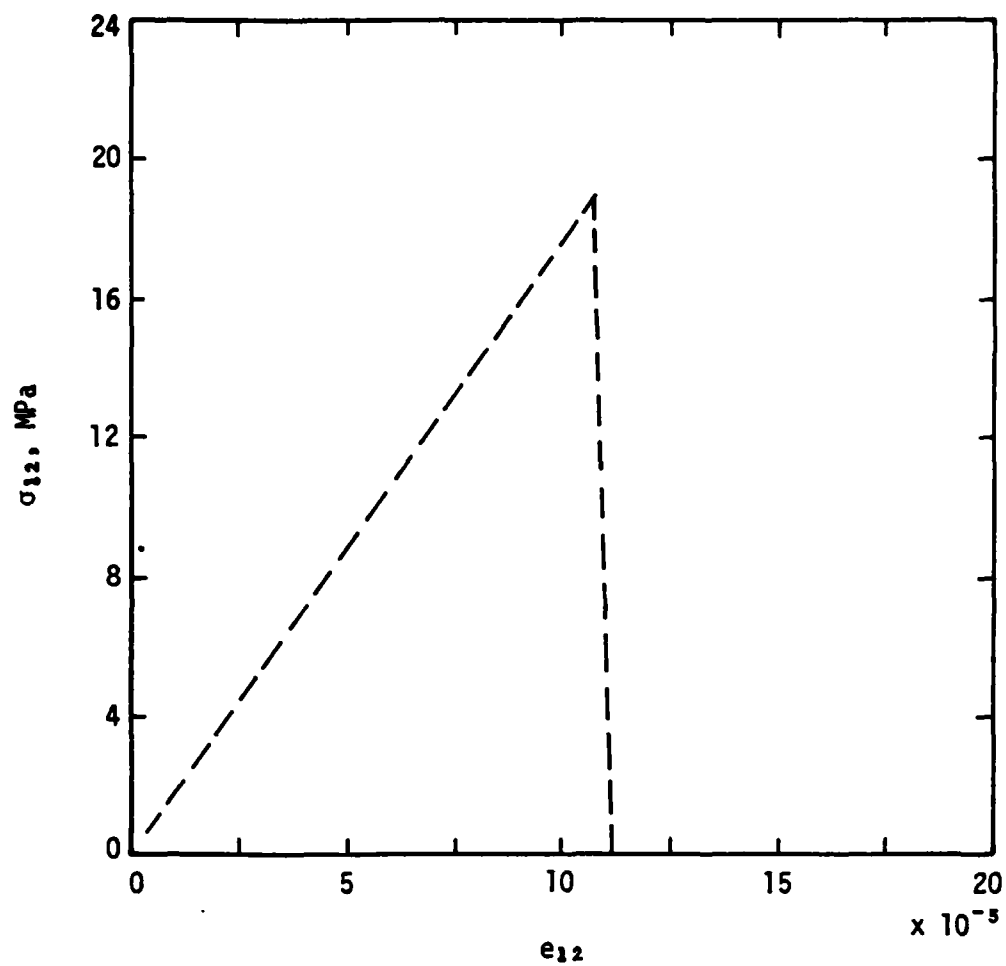


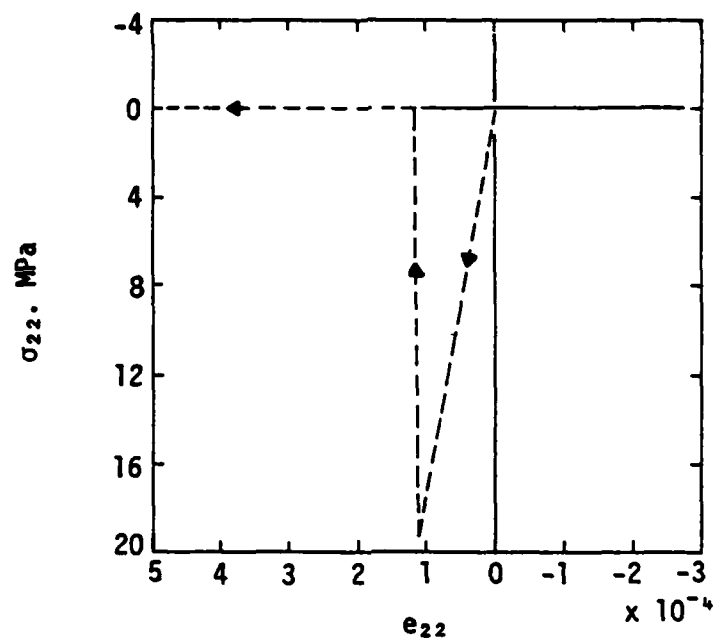
Figure 7. Cracking failure for shear stress versus shear strain.

Path 3, indirect shear (Figs. 8a and 8b)

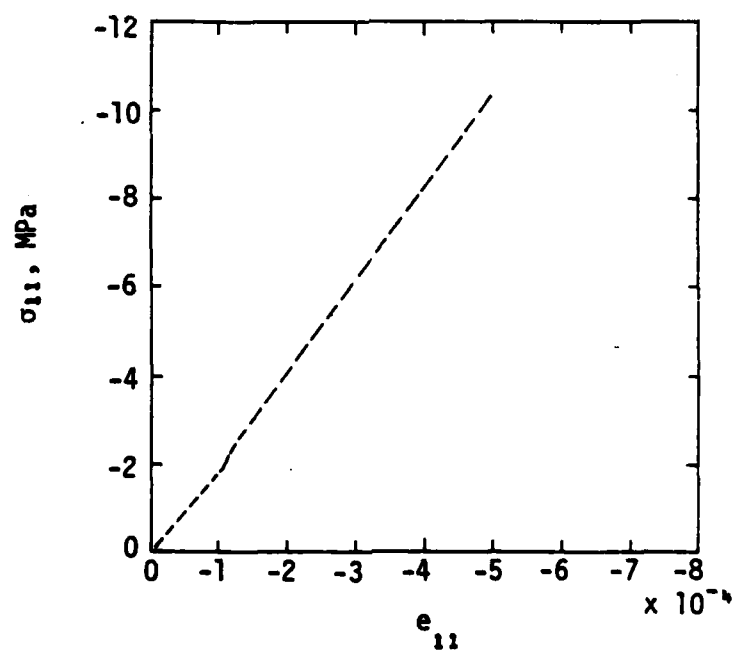
Here the first component of strain is decreased while the second component is increased by the same amount. The tensile component of stress displays the cracking phenomenon, which causes a simultaneous adjustment in the compressive stress when the stress redistribution occurs.

Although these examples represent elementary stress paths, they show that the algorithm is operational. The theory and numerical procedure can now be used as the basis for an in-depth engineering model investigation of the cracking of concrete. This investigation will provide guidelines to be used in seeking suitable experimental data.

Another important application involves interface models in which the possibility of separation is generally not considered. Instead, such models attempt to predict interface shear stress as a function of normal pressure and relative motion. For dynamic situations, separation is a distinct possibility. Therefore, a cracking algorithm must be combined with an interface model to provide a complete analytical capability.



(a) Tensile components.



(b) Compressive components.

Figure 8. Indirect shear response.

IV. INTERFACE MODELING

Coulomb's law describes frictional effects between rigid bodies subject to the gross sliding of one body relative to another. Because of its apparent conceptual simplicity, many engineers have attempted to apply the law point-wise to contact problems in continuum mechanics. Even for linearly elastic bodies, there are fundamental questions concerning the existence of solutions (Ref. 23). This lack of a proof of existence may be one of the reasons that no single frictional law has been generally accepted as providing results consistent with observations. For metallic surfaces, a nonlocal and nonlinear friction law is suggested (Ref. 23). It is possible that a similar law may be appropriate for interfaces between concrete and soils.

The study of interface phenomena is fraught with difficulties as indicated by the results presented in Reference 24. When a constant force is applied to one body in a direction parallel to an interface, a constant slip rate is often observed. However, in other cases that appear similar, a non-constant slip motion (stick-slip) is observed. It can be shown that this instability can occur if the stiffness of the moving body is less than a critical value that depends on the inertia of the body.

The possibilities of nonexistent solutions and instabilities are rarely considered in engineering models of interfaces. Some models suggest that the theory of plasticity be used to represent interfaces. These models appear to be superior to the conventional Coulomb model for several reasons. First, relative motion is observed for any tangential force. The plasticity model predicts this phenomenon; the Coulomb model does not. Second, hardening and softening are often observed, and these features are easily characterized by a plasticity model. Third, multidimensional features are easily incorporated in a plasticity model, whereas special rules must be constructed for the Coulomb model. As is shown, the plasticity formulation can also be incorporated in existing computer codes with a minimal degree of adjustment.

Ultimately any model must be verified by experimental data. Some data on concrete-soil interfaces exist (Ref. 25), although these data have apparently never been used for verification purposes. Reference 25 gives rather extensive results for both clay and sand, together with data that should permit these materials to be well defined.

The cited references indicate that several aspects of interface modeling are being investigated and that, as usual, a large disparity exists between important theoretical considerations and engineering models.

V. RECOMMENDATIONS

The primary emphasis in this work phase has been on developing an improved understanding of strain invariants and rate effects and on incorporating cracking into the constitutive model. Developments associated with strain invariants have been quite successful, and an engineering approach for representing cracking has been demonstrated, but questions about rate effects remain unanswered. The basis has been established for focusing now on specific topics that address fundamental questions concerning material behavior. The answers to these questions could provide an improved model. The topics to be addressed--rate effects in concrete, interface modeling, and the response of clay--have been selected on the basis of the general dearth of knowledge in these areas.

The experimental device proposed for ascertaining the multiaxial response of concrete under strain rates having a magnitude of the order of $1/s$ is described in Section II. The essential aspect of the device is that the combination of specimen size, strain rate magnitude, and loading rates obtained from explosives is uniquely appropriate in that all major criteria can be met.

The experimental equipment can help answer several fundamental questions. No information is available on whether dilatation increases or decreases with strain rate. The enhancement of strength with strain rate as a function of the ratios of principal stresses is not known. With a plasticity model, there is an open question concerning which of the hardening parameters--strain rate, inelastic strain rate, or stress rate--is most suitable for the theoretical formulation. Overall, it is believed that the theoretical basis is sufficiently advanced to provide sound guidelines for an important experimental program.

The observed interface behavior of a change in interface shear for any change in relative displacement before the limit state is reached is considerably different from the behavior implied by a Coulomb model. The use of the Coulomb model also has the implication of possible nonexistence of solutions. An interface model that incorporates newer mathematical concepts such as a nonlocal feature may be especially suitable for representing the roughness of concrete surfaces. Furthermore, such an approach may be helpful to the development of a robust numerical algorithm.

The viscoplastic model for representing frictional materials provides a reasonable basis for the exploration of new regimes of material behavior. It is recommended that the model be used as a basis for addressing fundamental research on problems concerning rate effects in concrete and soil-concrete interfaces.

REFERENCES

1. Mainstone, R. J., "Properties of Materials at High Rate of Straining or Loading," Materials and Structures, Vol. 8, No. 44, March-April 1975.
2. Kaplan, S. A., "Factors Affecting the Relationship Between Rate of Loading and Measured Compressive Strength of Concrete," Magazine of Concrete Research, Vol. 32, No. 111, June 1980.
3. Green, H., "Impact Strength of Concrete," Institution of Civil Engineers, Vol. 28, 1964, pp. 383-396.
4. Dhir, R. K., and Sangha, C. M., "A Study of the Relationships Between Time, Strength, Deformation, and Fracture of Plain Concrete," Magazine of Concrete Research, Vol. 24, No. 81, December 1972.
5. Suaris, W., and Shah, S. P., "Mechanical Properties of Materials Subjected to Impact," Introductory Report from the Symposium on Concrete Structures Under Impact and Impulsive Loading, Bundesanstalt für Materialprüfung, Berlin, Germany, June 2-4, 1982.
6. Reinhardt, H. W., "Testing and Monitoring Techniques for Impact and Impulse Loading of Concrete Structures," Introductory Report from the Symposium on Concrete Structures Under Impact and Impulsive Loading, Bundesanstalt für Materialprüfung, Berlin, Germany, June 2-4, 1982.
7. Atchley, B. L., and Furr, H. L., "Strength and Energy Absorption Capabilities of Plain Concrete Under Dynamic and Static Loadings," ACI Journal, November 1967, pp. 745-756.
8. Jones, P. G., and Richart, F. E., "The Effect of Testing Speed on Strength and Elastic Properties of Concrete," Proceedings of the American Society of Testing and Materials, Vol. 36, 1936, pp. 380-391.
9. Watstein, D., "Effect of Straining Rate on the Compressive Strength and Elastic Properties of Concrete," ACI Journal, April 1953, pp. 729-744.
10. Evans, R. H., "Effects of Rate of Loading on Some Mechanical Properties of Concrete," Mechanical Properties of Non-Metallic Brittle Materials, W. H. Walton, Ed., Butterworth, 1958, pp. 175-192.
11. Cowell, W. L., Dynamic Properties of Plain Portland Cement Concrete, Y-F008-08-03-401, DASA-13.0181, Naval Facilities Engineering and U.S. Naval Civil Engineering Laboratory, Port Hueneme, California, June 1966.
12. Goldsmith, W., Polivka, M., and Yang, T., "Dynamic Behavior of Concrete," Journal of Experimental Mechanics, February 1966, pp. 65-79.
13. Nicholas, T., An Analytical Study of the Split Hopkinson Bar Techniques for Strain-Rate Dependent Material Behavior, AFML-TR-71-155, Air Force Materials Laboratory, Wright-Patterson AFB, Ohio, August 1971.

REFERENCES (Continued)

14. Nicholas, T., Dynamic Tensile Testing of Structural Materials Using a Split Hopkinson Bar Apparatus, AFWL-TR-80-4053, Material Laboratory, Air Force Wright Aeronautical Laboratories, Wright-Patterson Air Force Base, Ohio, October 1980.
15. Spooner, D. C., "Stress-Strain-Time Relationships for Concrete," Magazine of Concrete Research, Vol. 23, No. 75-76, June-September 1971, pp. 127-131.
16. Hughes, B. P., and Gregory, R., "Concrete Subjected to High Rates of Loading in Compression," Magazine of Concrete Research, Vol. 24, No. 78, March 1972, pp. 25-36.
17. Sparks, P. R., and Menzies, J. B., "The Effect of Rate of Loading Upon the Static and Fatigue Strength of Plain Concrete in Compression," Magazine of Concrete Research, Vol. 25, No. 28, June 1973.
18. Hughes, B. P., and Watson, A. J., "Compressive Strength and Ultimate Strain of Concrete Under Impact Loading," Magazine of Concrete Research, Vol. 30, No. 105, December 1978.
19. Albertini, C., and Montagnani, M., "Testing Techniques in Dynamic Biaxial Loading," Proceedings of the Second Conference On the Mechanical Properties of Materials at High Rates of Strain, Oxford, England, March 28-30, 1979, Conf. Series No. 47.
20. Takeda, J., Tachikawa, H., and Fijimoto, K., Mechanical Properties of Concrete and Steel in Reinforced Concrete Structures Subjected to Impact or Impulsive Loadings, National Defense Academy, Yokosuka, Japan, 1981.
21. Bazant, Z. P., and Oh, B. H., "Strain Rate Effects in Rapid Triaxial Loading of Concrete," ASCE Journal of the Engineering Mechanics Division, Vol. 108, No. EM5, October 1982.
22. Building Code Requirements for Reinforced Concrete, ACI Standard 318-71, American Concrete Institute, 1971.
23. Oden, J. T., and Pires, E. B., "Nonlocal and Nonlinear Friction Laws and Variational Principles for Contact Problems in Elasticity," Journal of Applied Mechanics, Vol. 50, March 1983, pp. 67-76.
24. Rice, J. R., and Ruina, A. L., "Stability of Steady Frictional Slipping," Journal of Applied Mechanics, Vol. 50, June 1983, pp. 343-349.
25. Huck, P. J., et al., Dynamic Response of Soil/Concrete Interfaces at High Pressure, AFWL-TR-73-264, Air Force Weapons Laboratory, Kirtland Air Force Base, New Mexico, February 1974.

APPENDIX A*

A THIRD-INVARIANT PLASTICITY THEORY FOR LOW-STRENGTH CONCRETE

A theory of plasticity for frictional materials is developed in which first and third invariants of stress and strain are used instead of the more conventional second invariants. The usual concepts of strain-hardening plasticity are used with the exception that a nonassociated flow rule is required to control dilatation. A procedure for determining material parameters is outlined. For a weak concrete, detailed comparisons are made between theoretical and experimental stress-strain data for a large number of three-dimensional paths.

*This appendix is a reproduction of a professional paper submitted for publication in Journal of Engineering Mechanics (American Society of Civil Engineers). Thus it is a self-contained document with its own internally consistent numbering system for equations, references, and figures and with a format prescribed by the publisher.

A THIRD-INVARIANT
PLASTICITY THEORY FOR LOW-STRENGTH CONCRETE

Howard L. Schreyer,¹ M. ASCE, and Susan M. Babcock,² A.M. ASCE

September, 1983

INTRODUCTION

Numerous attempts have been made to model concrete with the theory of plasticity. Several models incorporate strain hardening, but none has achieved the generality and simplicity represented by the Von Mises isotropic hardening model used for metals. A corresponding theory, in which the first and third invariants of stress and strain are used instead of the second invariants, is developed here for frictional materials. Material parameters are chosen for a weak concrete, and detailed comparisons are made between theoretical and experimental stress-strain data for a large number of three-dimensional paths.

In the phenomenological approach to modeling a frictional material such as concrete, it is assumed that all essential response features can be represented in a tractable model without the explanation that would be provided by micromechanics. Such an approach is justified by the need to provide engineering analyses of constructed or planned systems. The resulting model should not violate basic principles and, as a deeper understanding is

¹Professor, Department of Mechanical Engineering, and Research Scientist, New Mexico Engineering Research Institute, University of New Mexico, Albuquerque, NM 87131.

²Research Engineer, New Mexico Engineering Research Institute, University of New Mexico, Albuquerque, NM 87131.

achieved, additional details should be incorporated easily within the framework. However, the current status of model development requires that the adequacy of a model be evaluated, not on a micromechanical basis, but on a macro-mechanical basis as represented by mechanical experiments on specimens in a laboratory. For concrete loaded in compression to the limit state, the general features exhibited include inelastic compaction under hydrostatic loading, shear enhanced compaction, dilatation, and strain hardening. These aspects of stress-strain behavior must be simulated realistically to obtain engineering solutions to a variety of boundary-value problems involving concrete structures.

Representative models for concrete are described in Refs. 1, 2, 3, and 8. Often the primary concern is the limit state, in which case an elastic-perfectly plastic approach is adequate (8). In other cases, the actual strain-hardening features are represented. Comparison with experimental data are often provided, but for the most part these data are of a restricted class, triaxial paths or biaxial paths in plane stress being the most common. As such, these data can provide only a limited evaluation of models.

In a recent set of experiments on cubical specimens, three-dimensional paths were prescribed (6). The paths varied from triaxial to multisegmental paths that provided transitions between uniaxial, biaxial, and proportional loadings. Each path was performed on two or three specimens. The results were evaluated and combined into single stress-strain curves for each path (7). Although principal axes of stress were held fixed, it is believed that these data can provide a more comprehensive evaluation of a model than that normally undertaken.

In Ref. 4 a third-invariant model for frictional materials is described, and an initial evaluation based on a comparison of theoretical and experimental data for two materials is provided. Analogous to the von Mises hardening theory, the model is an isotropic strain-hardening one; therefore, there are relatively few parameters. Thus, if the basic response features of concrete can be adequately represented, the model would be appropriate for use in large finite-element or finite-difference codes. An evaluation is provided by using a large number of paths for one material, rather than a few paths for several materials. In addition to the correlation between theoretical and experimental results, the procedure for choosing material parameters is described.

EXPERIMENTAL DATA

The triaxial testing device at New Mexico State University can apply, independently, loads on three faces of a cube so that all paths are stress-controlled. This device was used to obtain stress-strain data for a variety of paths (6). For each path these data were evaluated and condensed to representative curves (7), which can be used conveniently for evaluating constitutive models.

The tests were divided into three sets, the first two of which were constructed with all principal components of stress in compression. The last set, which will not be considered in this paper, involved a tensile component of stress for at least some portion of each path. Each test in the first set was performed on two specimens. The tests consisted primarily of conventional uniaxial, biaxial, triaxial, and shear tests. The second set of nine tests involved more complicated paths in the compressive regime; consequently, each test in this set was performed on three specimens.

To perform each experiment, it was necessary to give the stress paths in incremental form, which is also a convenient way to describe the paths analytically. Tables 1 and 2 provide a complete description of these paths in terms of a positive increment in stress, Δs . Each path is identified by a number and the set to which it belongs, and each segment of the path is described briefly. Terms are defined in the tables as necessary.

The paths are shown in Fig. 1 for the $\sqrt{J_2^T}$ -P plane where

$$P = -\frac{1}{3}(\sigma_1 + \sigma_2 + \sigma_3) \quad (1)$$

$$\sqrt{J_2^T} = \left\{ \frac{1}{6}[(\sigma_1 - \sigma_2)^2 + (\sigma_2 - \sigma_3)^2 + (\sigma_3 - \sigma_1)^2] \right\}^{1/2} \quad (2)$$

represent the mean pressure and the second invariant of the stress deviator. The principal stresses, σ_1 , σ_2 , and σ_3 , are assumed positive in tension. As these plots vividly demonstrate, the experiments cover a large spectrum of stress-defined paths.

Considering the complexity of the paths, a remarkable repeatability was obtained. Certain anomolous results were observed, however, and corrections were made for obvious shifts in strain data. All such adjustments are fully described in Ref. 7. After these adjustments were made, composite stress-strain curves were developed for each stress path. These data are given as the experimental curves shown in Fig. 2. To illustrate the large variations in stress and strain from one path to the next, the same scale is used for all the plots. To conserve space, any curve starting from the lower right corner is associated with the abscissa at the top of each plot. The variation of pressure with volumetric strain is a useful relation, but this information is implicit in Fig. 2.

TABLE 1. SET 1: STRESS PATHS IN COMPRESSION

| Path | Description |
|------|---|
| 1 | Uniaxial stress to failure $\Delta\sigma_1 = \Delta\sigma_2 = 0; \Delta\sigma_3 = -\Delta s$ |
| 2 | Uniaxial stress to failure. This and path 1 represent a test for initial anisotropy. $\Delta\sigma_1 = -\Delta s; \Delta\sigma_2 = \Delta\sigma_3 = 0$ |
| 3 | Biaxial stress to failure with $\sigma_2/\sigma_1 = 1.0; \sigma_3 = 0$ $\Delta\sigma_1 = -\Delta s; \Delta\sigma_2 = -\Delta s; \Delta\sigma_3 = 0$ |
| 4 | Hydrostatic loading followed by uniaxial loading to failure (i) $\Delta\sigma_1 = \Delta\sigma_2 = \Delta\sigma_3 = -\Delta s$ to the point $\sigma_1 = \sigma_2 = \sigma_3 = -8.5 \text{ MPa}$ (ii) $\Delta\sigma_1 = -\Delta s; \Delta\sigma_2 = \Delta\sigma_3 = 0$ |
| 5 | Hydrostatic loading followed by shear loading to failure (i) $\Delta\sigma_1 = \Delta\sigma_2 = \Delta\sigma_3 = -\Delta s$ to the point $\sigma_1 = \sigma_2 = \sigma_3 = -16.6 \text{ MPa}$ (ii) $\Delta\sigma_1 = -\Delta s; \Delta\sigma_2 = \Delta s; \Delta\sigma_3 = 0$ |
| 6 | 3-D stress to failure (subject to extensometer capability) with $\sigma_2/\sigma_1 = 1.0; \sigma_3/\sigma_1 = 0.1$ $\Delta\sigma_1 = -\Delta s; \Delta\sigma_2 = -\Delta s; \Delta\sigma_3 = -0.1 \Delta s$ |
| 7 | Biaxial stress to failure with $\sigma_2/\sigma_1 = 0.5; \sigma_3 = 0$ $\Delta\sigma_1 = -\Delta s; \Delta\sigma_2 = -0.5 \Delta s; \Delta\sigma_3 = 0$ |
| 8 | 3-D stress to failure (subject to extensometer capability) with $\sigma_2/\sigma_1 = 0.5; \sigma_3/\sigma_1 = 0.1$ $\Delta\sigma_1 = -\Delta s; \Delta\sigma_2 = -0.5 \Delta s; \Delta\sigma_3 = -0.1 \Delta s$ |

TABLE 2. SET 2: ADDITIONAL STRESS PATHS IN COMPRESSION

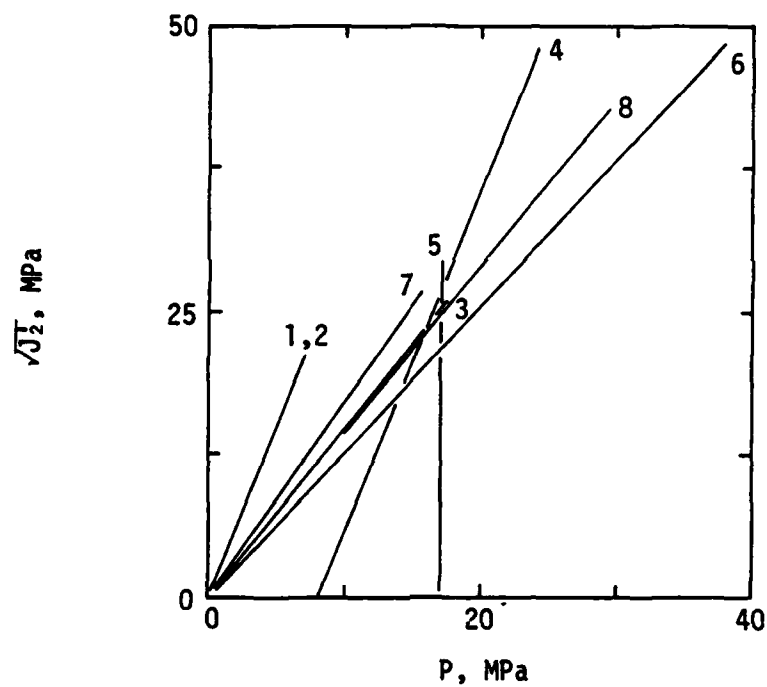
| Path | Description |
|------|---|
| 1 | (i) Load hydrostatically to $\sigma_1 = \sigma_2 = \sigma_3 = -2.2$ MPa $\Delta\sigma_1 = \Delta\sigma_2 = \Delta\sigma_3 = -\Delta s$ |
| | (ii) Load uniaxially to $\sigma_1 = -17.8$ MPa; $\sigma_2 = \sigma_3 = -2.2$ MPa $\Delta\sigma_1 = -\Delta s$; $\Delta\sigma_2 = \Delta\sigma_3 = 0$ |
| | (iii) Unload to $\sigma_1 = \sigma_2 = \sigma_3 = -2.2$ MPa; $\Delta\sigma_1 = \Delta s$; $\Delta\sigma_2 = \Delta\sigma_3 = 0$ |
| | (iv) Load biaxially in x_1 - x_2 plane to failure with $\sigma_2/\sigma_1 = 1.0$; $\sigma_3 = -2.2$ MPa $\Delta\sigma_1 = \Delta\sigma_2 = -\Delta s$; $\Delta\sigma_3 = 0$ |
| 2 | (i) Load hydrostatically to $\sigma_1 = \sigma_2 = \sigma_3 = -2.1$ MPa; $\Delta\sigma_1 = \Delta\sigma_2 = \Delta\sigma_3 = -\Delta s$ |
| | (ii) Load biaxially in x_1 - x_2 plane to failure with $\sigma_1/\sigma_2 = 1.0$; $\sigma_3 = -2.1$ MPa $\Delta\sigma_1 = \Delta\sigma_2 = -\Delta s$; $\Delta\sigma_3 = 0$ |
| 3 | (i) Load hydrostatically to $\sigma_1 = \sigma_2 = \sigma_3 = -2.0$ MPa $\Delta\sigma_1 = \Delta\sigma_2 = \Delta\sigma_3 = -\Delta s$ |
| | (ii) Biaxial stress in x_1 - x_2 plane to $\sigma_1 = \sigma_2 = -22.5$ MPa; $\sigma_3 = -2.0$ MPa $\Delta\sigma_1 = \Delta\sigma_2 = -\Delta s$; $\Delta\sigma_3 = 0$ |
| | (iii) Unload to $\sigma_1 = \sigma_2 = \sigma_3 = -2.0$ MPa; $\Delta\sigma_1 = \Delta\sigma_2 = \Delta s$; $\Delta\sigma_3 = 0$ |
| | (iv) Load uniaxially in x_1 -direction to failure $\Delta\sigma_1 = -\Delta s$; $\Delta\sigma_2 = \Delta\sigma_3 = 0$ |
| 4 | (i) Load hydrostatically to $\sigma_1 = \sigma_2 = \sigma_3 = -2.0$ MPa $\Delta\sigma_1 = \Delta\sigma_2 = \Delta\sigma_3 = -\Delta s$ |
| | (ii) Load uniaxially in x_1 -direction to failure $\Delta\sigma_1 = \Delta s$; $\Delta\sigma_2 = \Delta\sigma_3 = 0$ |

TABLE 2. CONTINUED

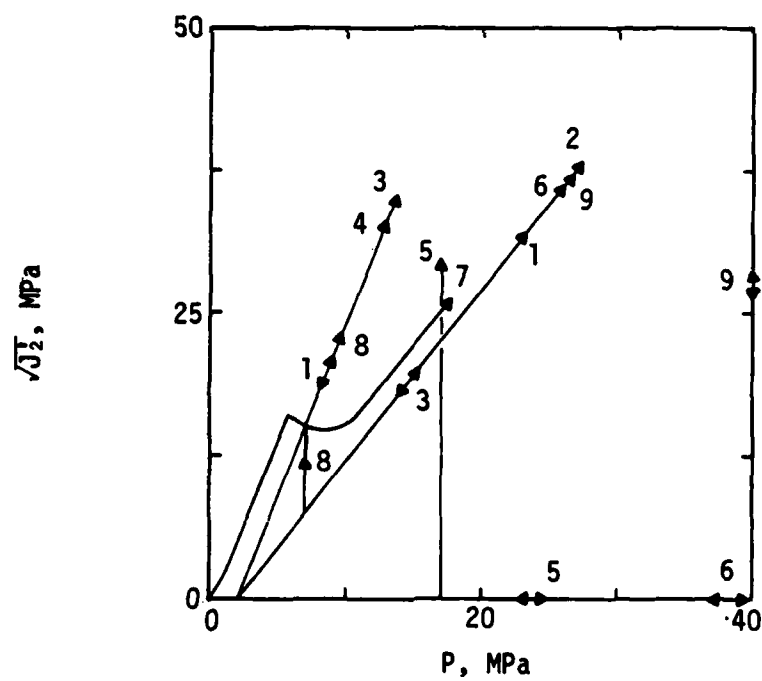
| Path | Description |
|------|---|
| 5 | (i) Load hydrostatically to $\sigma_1 = \sigma_2 = \sigma_3 = -26.2$ MPa $\Delta\sigma_1 = \Delta\sigma_2 = \Delta\sigma_3 = -\Delta s$ |
| | (ii) Unload hydrostatically to $\sigma_1 = \sigma_2 = \sigma_3 = -17.5$ MPa $\Delta\sigma_1 = \Delta\sigma_2 = \Delta\sigma_3 = \Delta s$ |
| | (iii) Load in shear to failure $\Delta\sigma_1 = -\Delta s; \Delta\sigma_2 = \Delta s; \Delta\sigma_3 = 0$ |
| 6 | (i) Load hydrostatically to $\sigma_1 = \sigma_2 = \sigma_3 = -40.0$ MPa $\Delta\sigma_1 = \Delta\sigma_2 = \Delta\sigma_3 = -\Delta s$ |
| | (ii) Unload hydrostatically to $\sigma_1 = \sigma_2 = \sigma_3 = -2.0$ MPa $\Delta\sigma_1 = \Delta\sigma_2 = \Delta\sigma_3 = \Delta s$ |
| | (iii) Load biaxially to failure $\Delta\sigma_1 = \Delta\sigma_2 = -\Delta s; \Delta\sigma_3 = 0$ |
| 7 | (i) Load biaxially to $\sigma_1 = \sigma_2 = -2.2$ MPa; $\sigma_3 = 0$ $\Delta\sigma_1 = \Delta\sigma_2 = -\Delta s; \Delta\sigma_3 = 0$ |
| | (ii) Load uniaxially to $\sigma_1 = -15.8$ MPa; $\sigma_2 = -2.2$ MPa; $\sigma_3 = 0$ $\Delta\sigma_1 = -\Delta s; \Delta\sigma_2 = \Delta\sigma_3 = 0$ |
| | (iii) Load to a biaxial state $\sigma_1 = \sigma_2 = -15.8$ MPa; $\sigma_3 = 0$ $\Delta\sigma_1 = \Delta\sigma_3 = 0; \Delta\sigma_2 = -\Delta s$ |
| | (iv) Load biaxially to failure $\Delta\sigma_1 = \Delta\sigma_2 = -\Delta s; \Delta\sigma_3 = 0$ |
| 8 | (i) Load hydrostatically to $\sigma_1 = \sigma_2 = \sigma_3 = -2.1$ MPa $\Delta\sigma_1 = \Delta\sigma_2 = \Delta\sigma_3 = -\Delta s$ |
| | (ii) Load uniaxially to $\sigma_1 = -17.6$ MPa $\Delta\sigma_1 = -\Delta s; \Delta\sigma_2 = \Delta\sigma_3 = 0$ |
| | (iii) Trace a path to $\sigma_1 = -2.1$ MPa; $\sigma_2 = -17.6$ MPa; $\sigma_3 = -2.1$ MPa $\Delta\sigma_1 = \Delta s; \Delta\sigma_2 = -\Delta s; \Delta\sigma_3 = 0$ |

TABLE 2. CONCLUDED

| Path | Description |
|------|---|
| 9 | (iv) Load uniaxially to failure $\Delta\sigma_1 = \Delta\sigma_3 = 0; \Delta\sigma_2 = -\Delta s$ |
| | (i) Load hydrostatically to $\sigma_1 = \sigma_2 = \sigma_3 = -40.0$ MPa $\Delta\sigma_1 = \Delta\sigma_2 = \Delta\sigma_3 = -\Delta s$ |
| | (ii) One cycle in shear |
| | (a) $\Delta\sigma_1 = \Delta s; \Delta\sigma_2 = -\Delta s; \Delta\sigma_3 = 0$ to $\sigma_1 = -21.0$ MPa $\sigma_2 = -59.0$ MPa; $\sigma_3 = -40.0$ MPa |
| | (b) $\Delta\sigma_1 = -\Delta s; \Delta\sigma_2 = \Delta s; \Delta\sigma_3 = 0$ to $\sigma_1 = \sigma_2 = \sigma_3 = 40.0$ MPa |
| | (iii) Unload hydrostatically to $\sigma_1 = \sigma_2 = \sigma_3 = -2.0$ MPa $\Delta\sigma_1 = \Delta\sigma_2 = \Delta\sigma_3 = \Delta s$ |
| | (iv) Load biaxially to failure $\Delta\sigma_1 = \Delta\sigma_2 = -\Delta s; \Delta\sigma_3 = 0$ |
| | |
| | |
| | |



(a) Set 1.



(b) Set 2.

Figure 1. Stress paths in $\sqrt{J_2}$ - P plane.

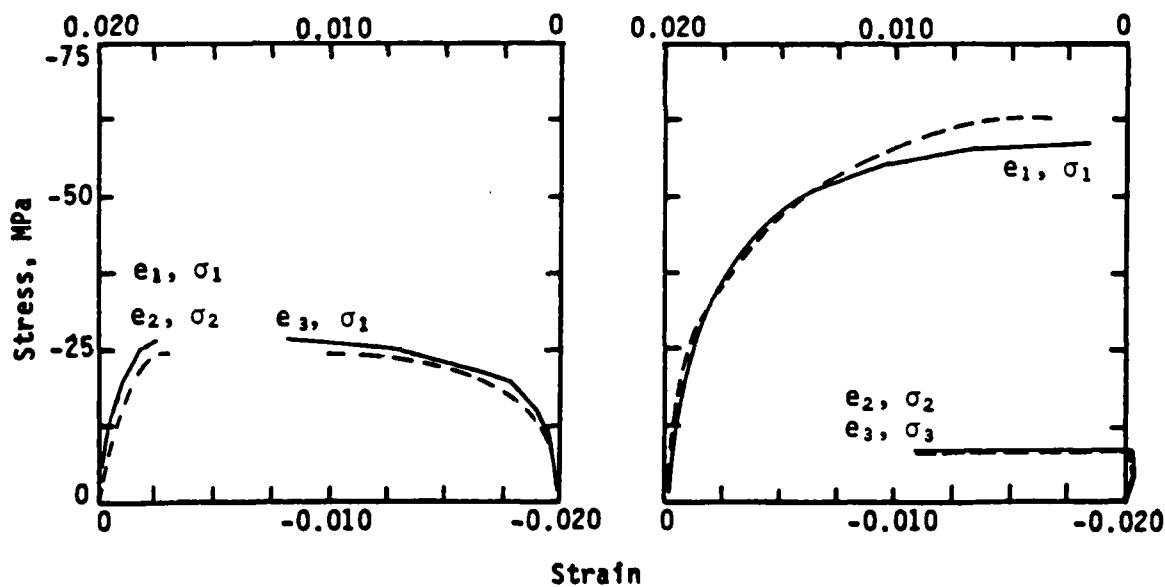
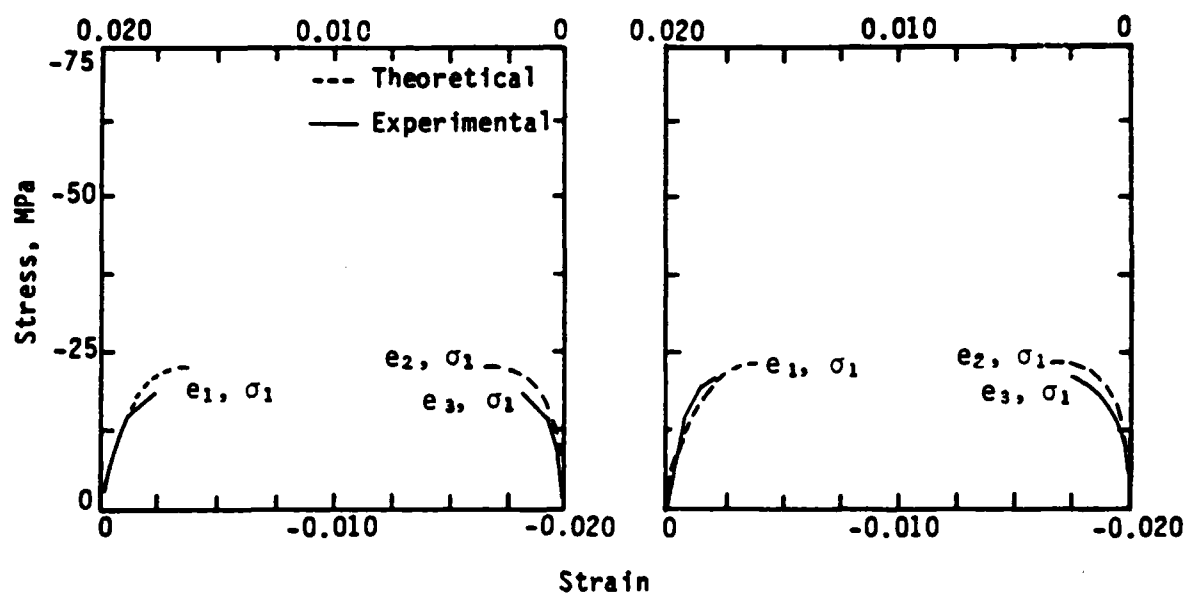


Figure 2. Theoretical and experimental stress-strain curves.

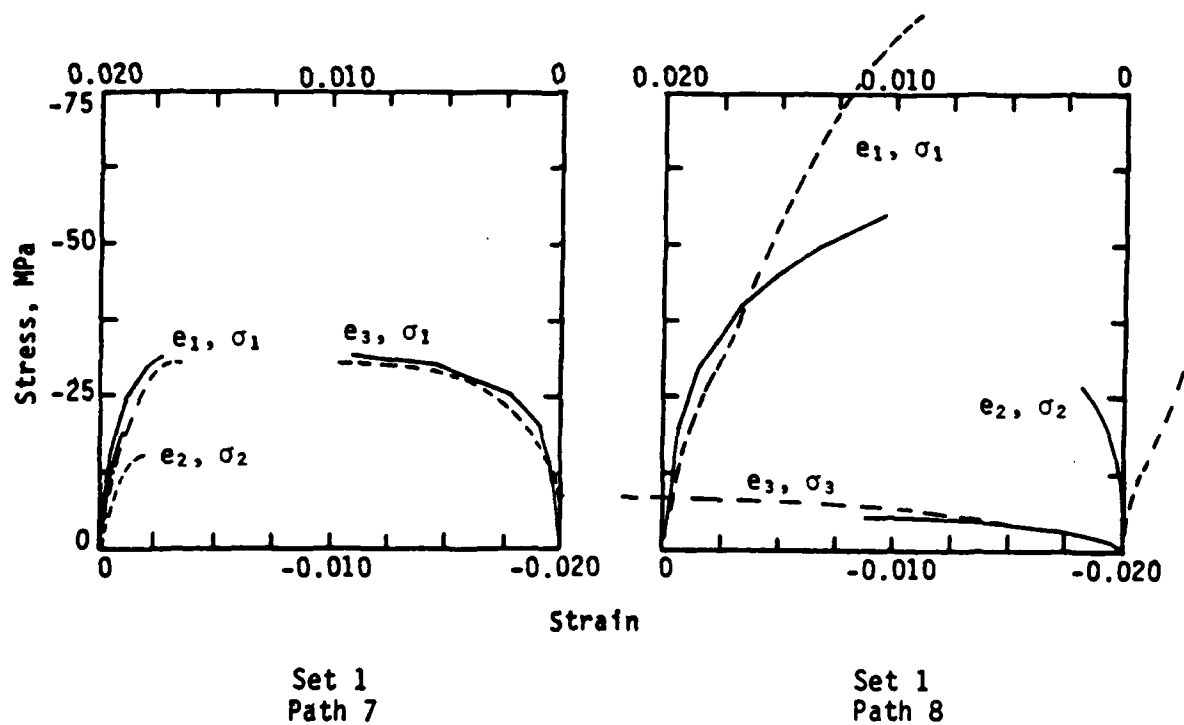
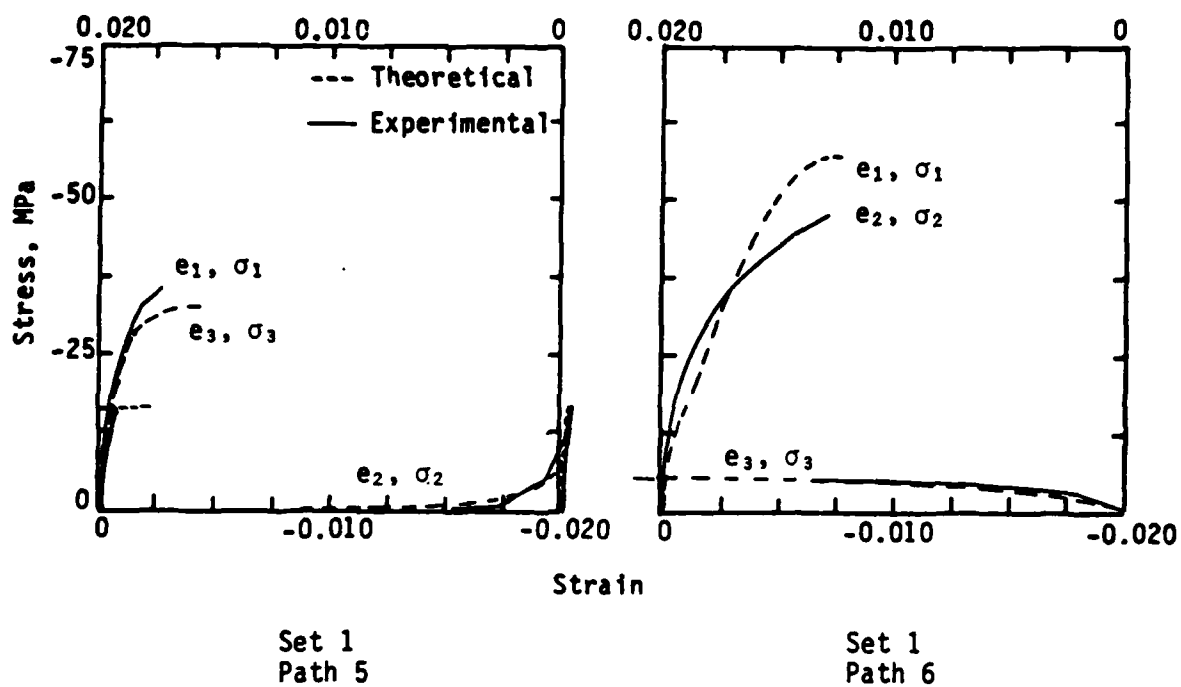
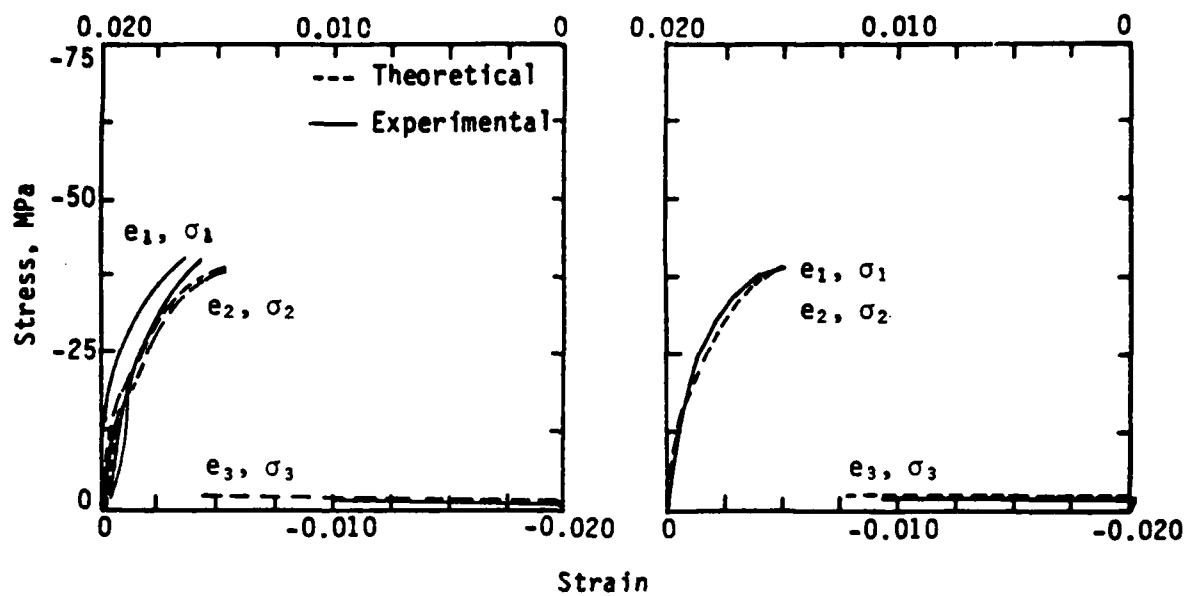
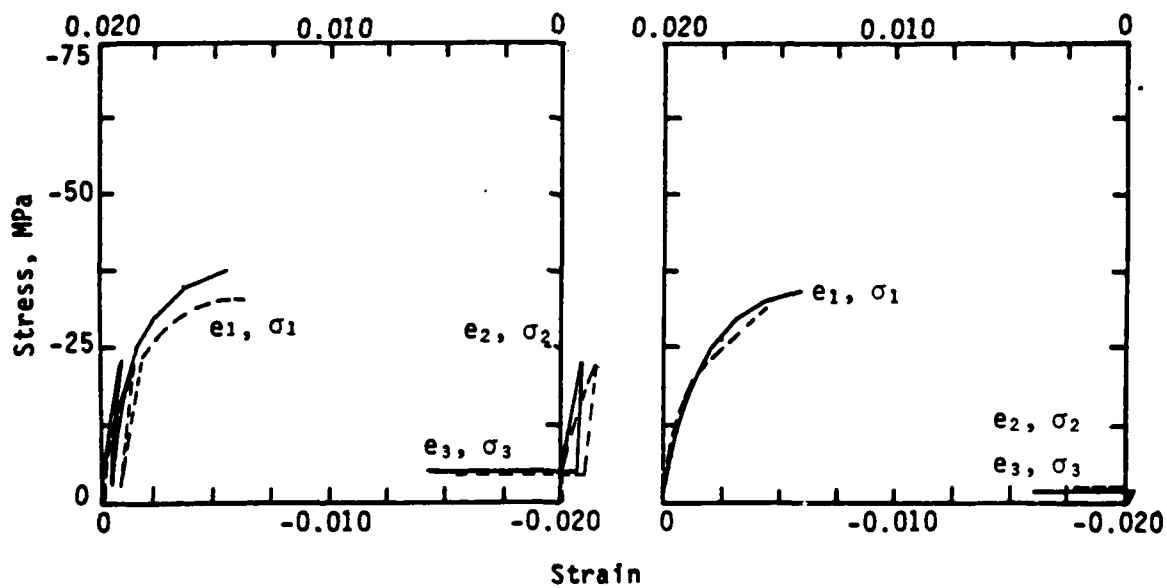


Figure 2. Continued.



Set 2
Path 1

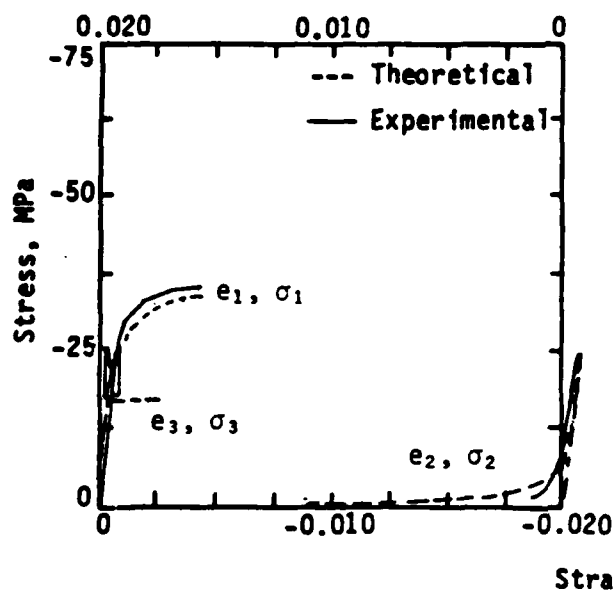
Set 2
Path 2



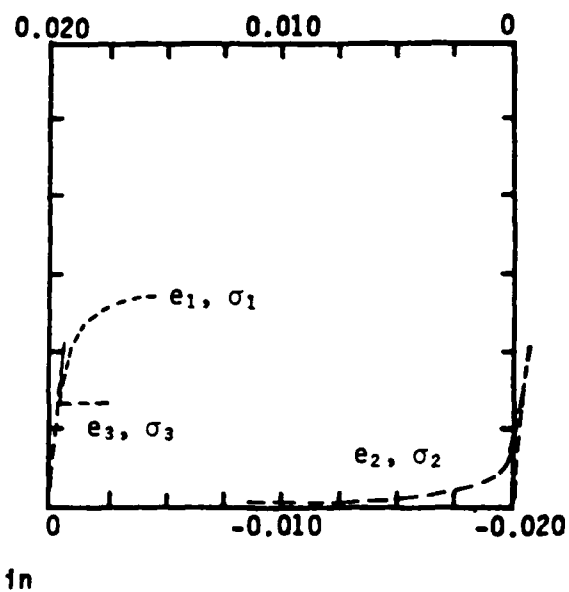
Set 2
Path 3

Set 2
Path 4

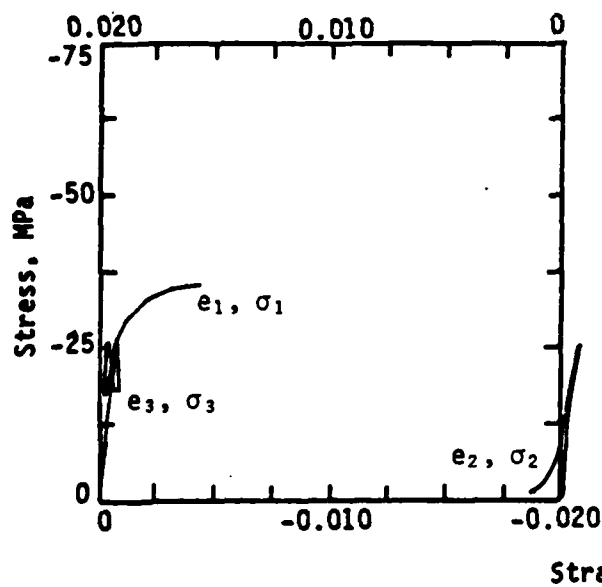
Figure 2. Continued.



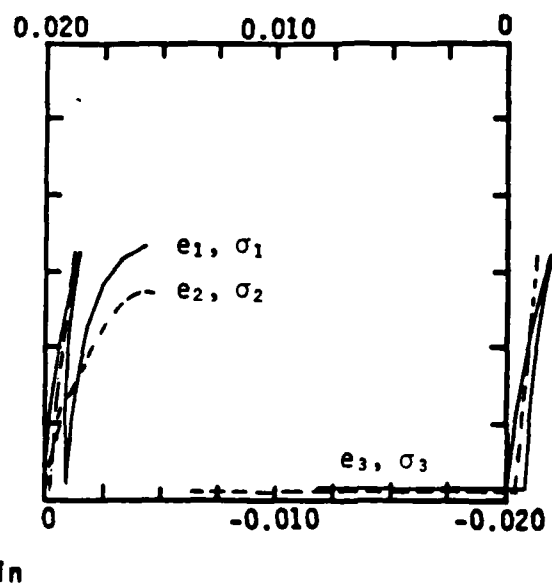
Set 2
Path 5



Set 2
Path 5
Theoretical
Only



Set 2
Path 5
Experimental
Only



Set 2
Path 6

Figure 2. Continued.

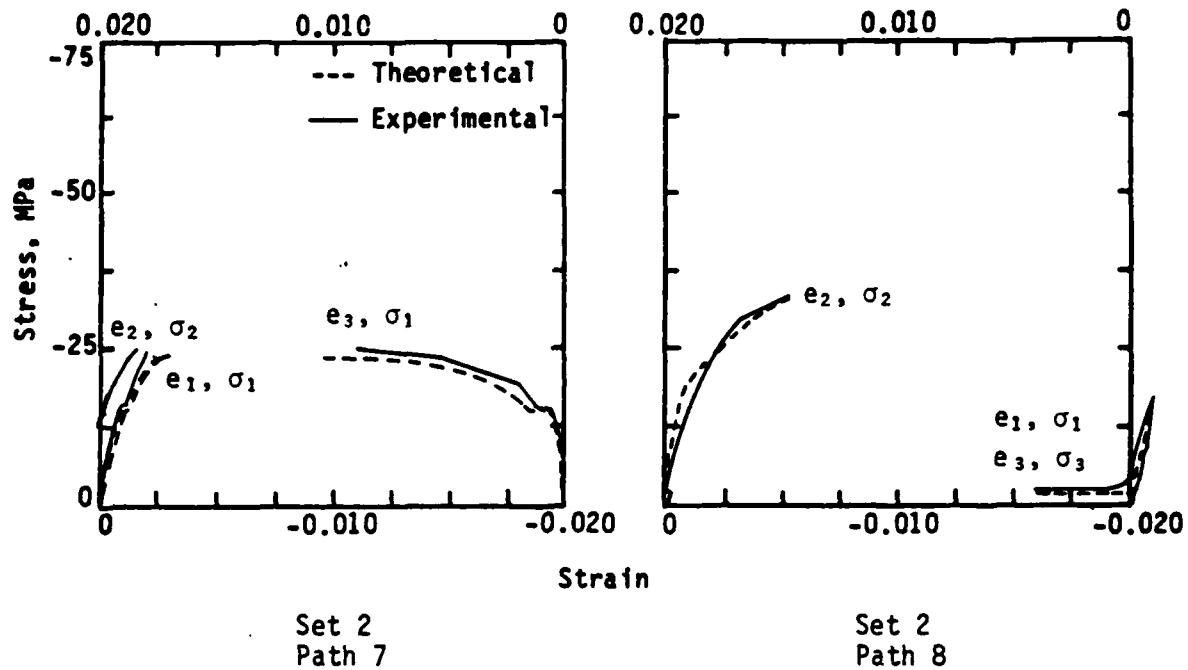


Figure 2. Continued.

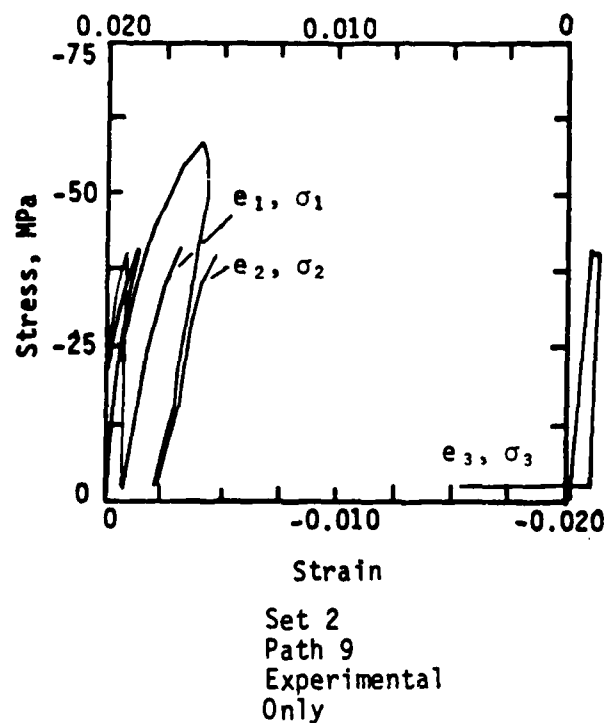
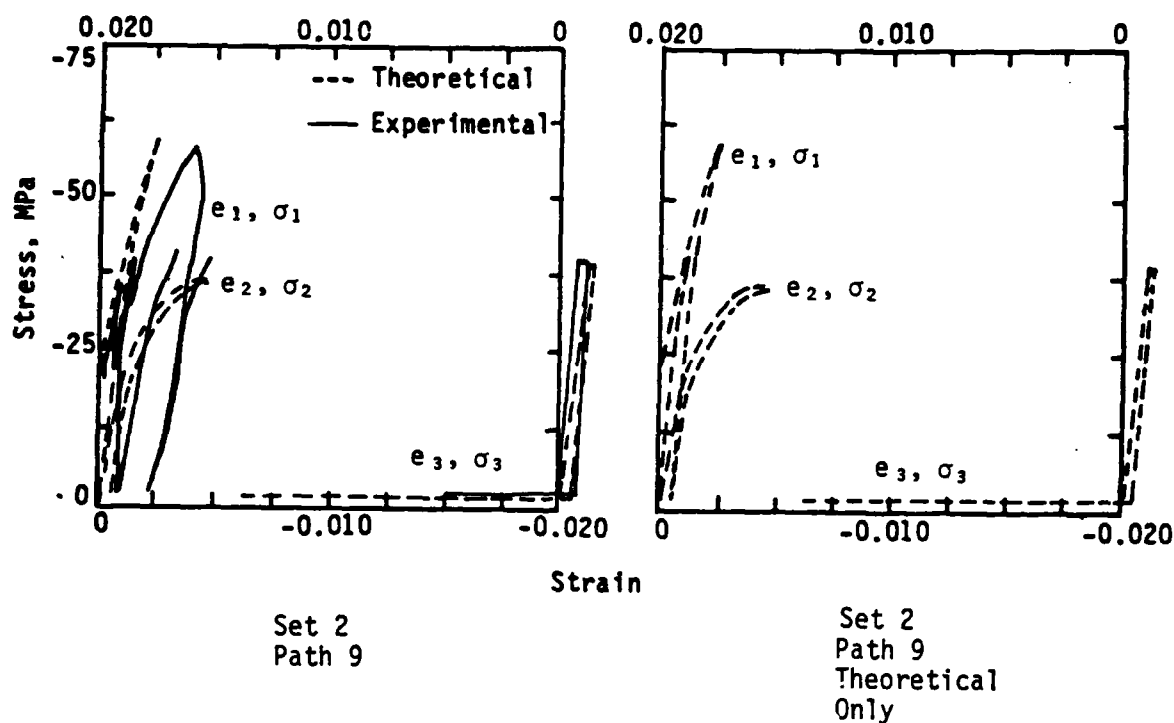


Figure 2. Concluded.

THIRD-INVARIANT MODEL

The third-invariant model has been described in Ref. 4, but the theory has been modified slightly since then. Thus, the formulation is outlined here but with more emphasis placed on the evaluation of material parameters.

A particular combination of the three stress invariants can also be considered a third invariant. On the basis of the use of a shifted stress concept, such an invariant is defined by

$$L = - [(\sigma_1 - \sigma_s)(\sigma_2 - \sigma_s)(\sigma_3 - \sigma_s) + \sigma_s^3]^{1/3} \quad (3)$$

in which the parameter σ_s can be defined as the cohesion and is assumed to vary with the deformation. On the basis of previous fits to experimental data, the limit surface is assumed to satisfy the relations

$$\sigma_s = \sigma_L \quad (4)$$

$$L = \gamma_L P - \sigma_L \quad (5)$$

Because limit point data for a set of paths are available, γ_L and σ_L can be obtained such that the limit line is an optimal fit in a least squares sense. For consistency, the value of σ_L must be chosen so that the value used in Eq. 3 agrees with the intercept value of the straight line defined by Eq. 5. Then γ_L is chosen to maximize the coefficient of correlation. The result of using the data of sets 1 and 2 is $\sigma_L = 1.87$ MPa and $\gamma_L = 0.79$, with a coefficient of correlation of 0.981. The corresponding fit is shown in Fig. 3.

The flow function is defined by

$$\phi = \gamma P - L - \sigma_s \quad (6)$$

so that the flow surface $\phi = 0$ is also a line in the L-P space. The strain-hardening functions γ and σ_s are assumed to be similar in form. As hardening

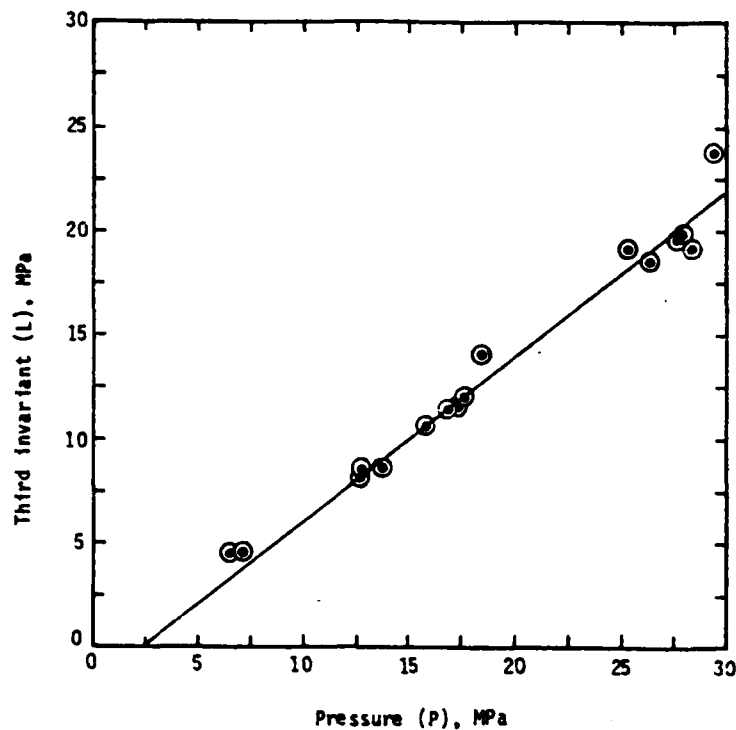


Figure 3. Straight-line fit to limit-point data.

occurs, γ decreases from an initial value of γ_0 to the limit value γ_L , while σ_s increases from σ_0 to σ_L . Softening is achieved by allowing γ to increase and σ_s to decrease after the limit state. The predicted response is not overly sensitive to the initial values, which are obtained by noting when nonlinearity first appears on a typical stress-strain path. These values were chosen to be $\gamma_0 = 2.5$ and $\sigma_0 = 1.0$ MPa.

To determine suitable functions for γ and σ_s , suppose that a path length strain invariant, \bar{e}^I , exists and that it has a unique value, \bar{e}_L^I , at the limit state no matter which path is followed. Appropriate strain-hardening functions that automatically provide the correct initial values of $\gamma = \gamma_0$ and

$\sigma_s = \sigma_0$ when $\bar{e}^i = 0$ and limit state values of $\gamma = \gamma_L$ and $\sigma_s = \sigma_L$ when $\bar{e}^i = \bar{e}_L^i$ are then given by

$$\gamma = \gamma_0 + (\gamma_L - \gamma_0) \sin \frac{\pi}{2} \left(\frac{\bar{e}^i}{\bar{e}_L^i} \right)^n \quad (7)$$

$$\sigma_s = \sigma_0 + (\sigma_L - \sigma_0) \sin \frac{\pi}{2} \left(\frac{\bar{e}^i}{\bar{e}_L^i} \right)^n \quad (8)$$

The parameter n is chosen to provide a reasonable shape for the strain-hardening portion of the predicted stress-strain curves. A value of $n = 0.16$ was considered appropriate for the weak concrete on the basis of comparisons between theoretical and experimental stress-strain curves.

Because an associated flow rule provides too much dilatation, a potential function of the following form is used:

$$\phi^* = \gamma^* p - L - \sigma_s \quad (9)$$

where

$$\gamma^* = \gamma + b \quad (10)$$

and b is a material constant. A nonassociated flow rule implies that the inelastic strain increment is given by

$$\begin{aligned} d\bar{e}^i &= d\lambda \frac{\partial \phi^*}{\partial \sigma} \\ &= d\lambda \left(\frac{\partial \phi}{\partial \sigma} + b \frac{\partial p}{\partial \sigma} \right) \\ &= d\lambda \left(\frac{\partial \phi}{\partial \sigma} - \frac{b}{3} \underline{I} \right) \end{aligned} \quad (11)$$

in which $d\lambda$ is a positive parameter, and $\underline{\sigma}$ and \underline{I} denote the stress and identity tensors, respectively. The implication of this equation is that dilatation

is reduced from that given by the associated flow rule if b is positive. For hydrostatic compaction with $P \gg \sigma_s$, it follows that $L \approx P$, and the volumetric inelastic strain increment is given by

$$\begin{aligned} de_v^i &= \text{trace } de^i \\ &= d\lambda(1 - \gamma - b) \end{aligned} \quad (12)$$

The requirement that such a loading path should always yield compaction is satisfied if $b > 1 - \gamma_L$. The easiest way to determine b is to monitor the lateral strains on a typical triaxial loading path and to adjust b to provide the type of fit desired for an ensemble of such paths. Here, the value of $b = 0.35$ was obtained.

An appropriate form for \bar{e}^i is still open to question, but such a form must include a volumetric effect if inelasticity is to be obtained for hydrostatic loading. Both compaction and dilatation can occur; therefore, an absolute value is used to obtain the path length increment of the first invariant:

$$d\bar{e}_1^i = \left| \text{tr } de^i \right| \quad (13)$$

Because the second-invariant increment is so useful for the theory of metal plasticity, it is included as follows:

$$d\bar{e}_2^i = [\text{tr}(de^{id})^2]^{1/2} \quad (14)$$

in which de^{id} denotes an increment in the inelastic strain deviator.

For the sake of generality a third invariant increment is also introduced, with the absolute value used to ensure a monotonically increasing parameter:

$$d\bar{e}_3^i = \left| \det(d\bar{e}^i) \right|^{1/3} \quad (15)$$

An increment in a path length invariant for frictional materials is assumed to be

$$de^{i*} = c_1 d\bar{e}_1^i + c_2 d\bar{e}_2^i + c_3 d\bar{e}_3^i \quad (16)$$

where c_1 , c_2 , and c_3 are material parameters. For any path, it is possible to determine the value of \bar{e}^{i*} at the limit point; the limit value is denoted by \bar{e}_L^{i*} . If the invariant \bar{e}^{i*} is to provide a useful plasticity theory, then \bar{e}_L^{i*} should be the same for all paths. Data such as those provided in Refs. 6 and 7 can be used to determine whether or not \bar{e}_L^{i*} is unique for a given material. In fact, when these data are used, values for \bar{e}_L^{i*} vary by an order of magnitude no matter which values are chosen for c_1 , c_2 , and c_3 . However, a distinguishing feature does appear: for those paths associated with large P , \bar{e}^{i*} is much larger than the value obtained for uniaxial stress. This dependence on P suggests that the definition of the third invariant should involve a weighting function. On the basis of a preliminary evaluation (5), the following form for an increment is proposed:

$$d\bar{e}^i = d\bar{e}^{i*} \frac{P_0}{P + P_0} \quad (17)$$

Here, the constant P_0 controls the effect of mean stress. If P_0 is large, the effect of P is minimal; the reverse is true if P is small.

The use of \bar{e}^i rather than \bar{e}^{i*} produces a dramatic reduction in the variation of values for \bar{e}^i at the limit state, suggesting that the parameters c_1 , c_2 , c_3 , and P_0 can be adjusted to minimize this variation. Because the nature

of the data hardly warrants a formal minimization procedure, a simple search procedure was instigated in which one parameter was adjusted at a time. With the arbitrary choice of $c_1 = 1$, the resulting values for the other parameters are $P_0 = 7$ MPa, $c_2 = 0$, and $c_3 = 0.5$. The interesting implication of $c_2 = 0$ is that only the first and third invariants of strain are necessary, which provides a nice correlation with the use of the first and third invariants of stress.

The resulting values for $\bar{\epsilon}_L^i$ at the limit states for all paths are given in Table 3. At first glance the variation still appears to be exceedingly large, although if one or two anomalous points such as paths 3 and 7 of set 2 are excluded, this variation is reduced considerably. Paths 1 and 2 of set 1 are both uniaxial stress paths, which were performed to check anisotropy by testing along different axes on two specimens from the same batch. The corresponding values of $\bar{\epsilon}_L^i$ differ by a factor of 2. It was also noted by Traina (6) that at the limit points, the strains were increasing at a significant rate and that it was difficult to identify closely the strains at the limit point. Furthermore, the data were obtained directly in digital form at each of approximately ten steps for each path. This digitizing can introduce significant error through the numerical sum used to approximate the integral for $\bar{\epsilon}_L^i$. For these reasons, more sophisticated approaches to evaluating P_0 and c_3 from these data are unwarranted. Furthermore, it appears that predicted results are not overly sensitive to $\bar{\epsilon}_L^i$; therefore, a representative value of $\bar{\epsilon}_L^i = 0.0025$ was selected.

On the basis of a combination of classical approaches and initial loading characteristics, the remaining parameters of Young's modulus and Poisson's ratio were chosen to be $E = 21,000$ MPa and $\nu = 0.25$, respectively.

TABLE 3. VALUES OF THE STRAIN INVARIANT \bar{e}^i AT LIMIT POINTS

| Path | \bar{e}_L^i (set 1) | \bar{e}_L^i (set 2) |
|------|-----------------------|-----------------------|
| 1 | 0.0014 | 0.0032 |
| 2 | 0.0026 | 0.0018 |
| 3 | 0.0032 | 0.0039 |
| 4 | 0.0030 | 0.0025 |
| 5 | 0.0014 | 0.0030 |
| 6 | 0.0017 | 0.0027 |
| 7 | 0.0026 | 0.0009 |
| 8 | 0.0023 | 0.0029 |
| 9 | --- | 0.0019 |

RESULTS

With the material parameters identified in the previous section, theoretical predictions of strain were made for the stress paths listed in Table 1. These results are shown with the experimental data in Fig. 2. In general, the correlation is good considering that the model is that of isotropic strain-hardening plasticity.

Variations between theoretical and experimental values of peak stress are a direct consequence of how well the straight line of Fig. 3 fits the limit state data. Corresponding variations in strain at the limit state are reflected to a considerable extent in how well the invariant \bar{e}^i captures the physical phenomena. Strains at the limit state are also affected by the path; therefore, agreement is contingent on a faithful representation through the strain-hardening portion of the path history.

The largest discrepancy occurs for the proportional loading case given as path 8 of set 1. The predicted peak stress is much higher than the experimental value even though the limit condition is satisfied. The reason is that in the L-P plane, a proportional path such as this one is almost parallel to the limit line so that a slight variation is magnified considerably. If the limit line were curved rather than straight, the discrepancy might be removed. Also, the measured intermediate strain is positive (tensile), whereas the predicted strain is negative. A similar feature is displayed to a lesser extent for path 5, sets 1 and 2. The reason is that the shape of the flow surface in the π -plane, as defined implicitly through the flow condition $\phi = 0$, is not as accurate as that proposed by Willam and Warnke (8). In other words, an error is introduced when a simplified model is used. Whether or not the error is significant depends on the intended application. To illustrate the point further, suppose path 8 of set 1 is altered so that the intermediate stress is 0.25 times the primary stress. This alteration corresponds to a slightly different radial line in the π -plane. The model predicts essentially zero intermediate strain as shown in Fig. 4 so that the theoretical ratio of 0.25 is the transition value between positive and negative intermediate strains. The higher value indicated by the experimental data may be the result of small shear stresses on the loaded faces of the specimens.

The next most important discrepancy involves the amount of inelastic deformation under hydrostatic loading as shown, for example, in the first part of path 9, set 2. The predicted inelastic volumetric strain is less than the experimental strain. Also, upon unloading, the model always predicts an elastic response, whereas some inelastic deformation is displayed in the tests. A kinematic hardening aspect would have to be added to the model to enable it to predict such a response feature.

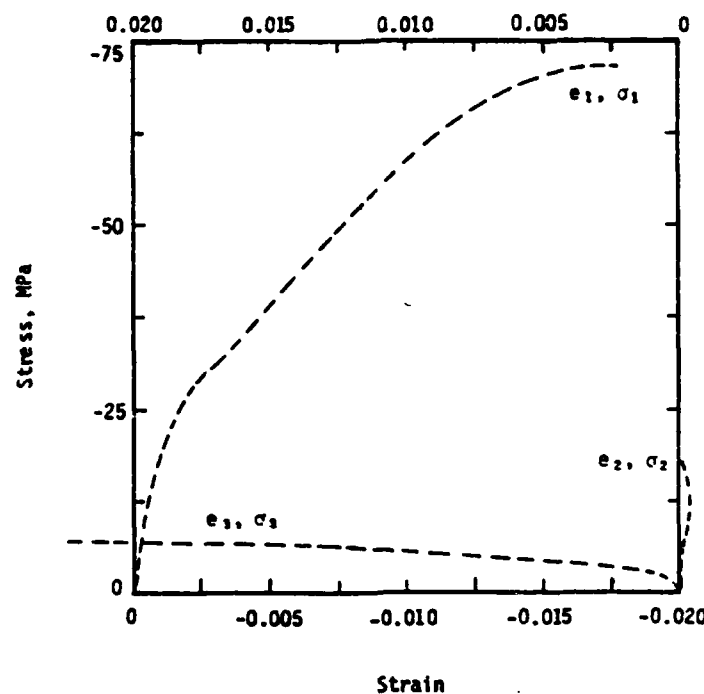


Figure 4. Theoretical prediction for triaxial loading with $\sigma_2 = 0.25\sigma_1$ and $\sigma_3 = 0.1\sigma_1$.

For all other cases it is believed that the agreement is more than adequate for the purposes of most engineering analyses.

CONCLUSION

These results show that there is considerable merit in the use of a strain-hardening isotropic plasticity model for representing the essential features of concrete behavior in the compressive regime. The study indicates that the first and third invariants of stress and strain more appropriately represent concrete than do the second invariants, which are commonly used for metal plasticity. A nonassociated flow rule is necessary to control dilatation.

Several aspects of concrete behavior have not been considered. Among these are tensile behavior, strain softening, and rate effects. The current

theory has been extended to incorporate these effects, but until more multi-axial experimental data become available, no definitive evaluation can be made. The primary advantage of the extended model is that it provides good guidelines for developing experimental apparatus with appropriate instrumentation.

Because the formulation is patterned after correspondingly attractive models used for metals, a constitutive equation algorithm can easily be added to existing computer codes. The model implicitly incorporates features such as inelastic hydrostatic compaction, shear enhanced compaction, dilatation, and strain-hardening. For those engineering applications in which a prediction of deformation is essential, this theory provides a balanced approach between accuracy and computational feasibility. Although the results of this work are restricted to low strength concrete, the model should be practicable for other concretes and geological materials.

ACKNOWLEDGMENTS

Many of the calculations were performed by D. Hayden. The support of the Air Force Office of Scientific Research is greatly appreciated.

REFERENCES

1. Bazant, Z. P., and Kim, S. S., "Plastic-Fracturing Theory for Concrete," ASCE J. Eng. Mech. Div., 105, pp. 407-428, June 1979.
2. Dragon, A., and Mroz, F., "A Continuum for Plastic-Brittle Behavior of Rock and Concrete," Int. J. Engng. Sci., Vol. 17, pp. 121-137, 1979.
3. Hsieh, S. S., Ting, E. C., and Chen, W. F., "A Plastic-Fracture Model for Concrete," International Journal of Solids & Structures, Vol. 18, pp. 181-197, 1982.

4. Schreyer, H. L., "A Third-Invariant Plasticity Theory for Frictional Materials," J. Structl. Mech., 11(2), 177-196, 1983.
5. Schreyer, H. L., "The Use of Third Invariants in a Plasticity Model for Frictional Materials," Transactions of the 7th International Conference on Structural Mechanics in Reactor Technology, Vol. L, Aug. 22-26, 1983, pp. 63-68.
6. Traina, L. A., Experimental Stress-Strain Behavior of a Low-Strength Concrete Under Multiaxial States of Stress, AFWL-TR-82-92, Air Force Weapons Laboratory, Kirtland Air Force Base, New Mexico, January 1983.
7. Traina, L. A., Babcock, S. M., and Schreyer, H. L., Reduced Experimental Stress-Strain Results for a Low-Strength Concrete Under Multiaxial States of Stress, AFWL-TR-83-3, Air Force Weapons Laboratory, Kirtland Air Force Base, New Mexico, May 1983.
8. Willam, K. J., and Warnke, E. P., "Constitutive Model for the Triaxial Behavior of Concrete," International Association of Bridges and Structures Subjected to Triaxial Stresses, Paper III - 1, Institute Sperimentali Modelli e Structure, Bergamo, Italy, May 17-19, 1974.

NOTATION

- b = material parameter;
 c_1, c_2, c_3 = material parameters;
 $d\lambda$ = material parameter;

E = Young's modulus;
 e_1, e_2, e_3 = principal strains;
 e_v^i = inelastic volumetric strain;
 \bar{e}^i = path length strain invariant;
 \bar{e}^{i*} = path length strain invariant;
 \bar{e}_L^i = path length strain invariant limit value;
 \underline{e}^i = inelastic strain tensor;
 \underline{e}^{id} = inelastic deviatoric strain tensor;
 \underline{I} = identity tensor;
 J_2 = second invariant of the stress deviator;

 L = stress invariant;
 n = material parameter;
 P = mean pressure;
 P_0 = material parameter with units of pressure;
 γ = slope of flow surface in L-P space;
 γ_L = slope of limit surface in L-P space;
 γ_0 = initial slope of flow surface in L-P space;
 γ^* = slope of potential function in L-P space;
 Δs = positive increment in stress;
 ν = Poisson's ratio;
 σ_L = cohesion at limit surface;
 σ_s = cohesion;
 σ_0 = initial cohesion;
 $\sigma_1, \sigma_2, \sigma_3$ = principal stresses;
 $\underline{\sigma}$ = stress tensor;
 ϕ = flow function; and
 ϕ^* = potential function.

APPENDIX B*

A THIRD-INVARIANT VISCOPLASTICITY THEORY FOR RATE-DEPENDENT SOILS

A theory of viscoplasticity for frictional materials is developed in which first and third invariants of stress and strain are used instead of the more conventional second invariants. Rate effects are incorporated directly into the expression for the flow surface so that the numerical algorithm for a plasticity subroutine can be used. The usual concepts of strain- and strain rate-hardening viscoplasticity are used except that a nonassociated flow rule is required to control dilatation. For two sandy materials, detailed comparisons are made of theoretical and experimental stress-strain data for both static and dynamic paths.

*This appendix is a reproduction of a professional paper submitted for publication in Journal of Engineering Mechanics (American Society of Civil Engineers). Thus it is a self-contained document with its own internally consistent numbering system for equations, references, and figures and with a format prescribed by the publisher.

A THIRD-INVARIANT VISCOPLASTICITY THEORY FOR RATE-DEPENDENT SOILS

Howard L. Schreyer,¹ M. ASCE, and James E. Bean,² M. ASCE

October 1983

INTRODUCTION

Large strain rates in soils arise in a number of situations that include strong seismic motion, pile driving, and high-explosive testing. Displacements as a function of time for points in the earth close to these disturbances are frequently required, and in these cases the constitutive model of the ground media must include rate effects. With modern computer codes, three-dimensional analyses are feasible. Thus, the model must be quite general but at the same time sufficiently simple so that storage and computation time requirements are reasonable for numerical computations. Proposed in this paper is a three-dimensional engineering model that provides a balance between accuracy and computational efficiency. Material parameters are selected, and detailed comparisons between theoretical and experimental stress-strain data are given for a sand and a clayey sand subjected to both static and dynamic loads.

The rate effect known as creep involves a relatively large time scale. The rate effect of interest here occurs over a short time and is characterized by an apparent enhancement of soil stiffness and strength. Materials exhibit both types of rate effects, although the characteristic times can vary widely.

¹Professor, Department of Mechanical Engineering, and Research Associate, New Mexico Engineering Research Institute, University of New Mexico, Albuquerque, NM 87131.

²Research Engineer, New Mexico Engineering Research Institute, University of New Mexico, Albuquerque, NM 87131.

Consequently, statements have been made to the effect that particular materials, such as sandy soils, are rate-independent. However, when the strain rate is large enough, a significant change from static behavior is observed even in these materials.

Jackson et al. (4) at the Waterways Experiment Station (WES) performed a set of static and dynamic tests on a clayey sand. The three principal components of stress and strain were measured in the static tests, and the resulting data are invaluable for the assessment of constitutive models. In the dynamic tests, which were uniaxial strain tests, the lateral stresses were not measured; therefore, these data are not as complete as desired. The fact remains, however, that these data are unique because so little is available in the way of experimental data. An exception is a paper by Ito and Fujimoto (3) in which experimental results are given for sand subjected to triaxial path tests. Because characteristic strain rates for these two test programs vary from 1/s (3) to 200/s (4), the data from these experiments provide a severe test for a constitutive model.

Various cap models have evolved from the original work of Drucker et al. (2), and considering the simplicity of the cap formulation, predictions are remarkably good. However, as the three-dimensional response features of soils have become better understood, the models have had to be modified. Nelson et al. (7) showed how a hardening law could be established to control dilatation, among other features. This approach has been extended by Baladi and Rohani (1) to a viscoplastic form that represents a generalization of a theory given by Perzyna (8).

The cap models are generally formulated in terms of the first and second invariants of stress and strain, which implies that the shape of the limit surface in the π -plane is circular. However, it is believed (6) that for geological materials the limit surface is triangular rather than circular; therefore, a more accurate theory necessary, and the third invariant of stress must be used in addition to the other two. This complication has been obviated to a certain extent by the observation of Lade and Duncan (6) that equally adequate predictions of limit states can be obtained by using only the first and third invariants. This idea has been developed by Lade (5) and more recently by Schreyer (11), who have used various forms of the third invariant. Schreyer and Babcock (12) have extended the concept to a more conventional strain-hardening formulation in which a single path-length strain invariant is shown to represent adequately a variety of paths for a weak concrete. Their basic formulation is shown here to be suitable for sandy soils as demonstrated by comparisons of theoretical and experimental data. In addition, the theory has been extended to viscoplasticity, but by means of an approach that differs considerably from that used by Baladi and Rohani (1). Instead of using a viscosity parameter, the approach outlined here involves describing the flow surface in terms of total strain rate (9). The use of the total strain rate provides an enhanced region of elastic response. The sets of experimental data that involve rate effects are used to evaluate the model.

THIRD-INVARIANT MODEL

The model described in Ref. 11 has been modified to incorporate rate effects. For the sake of completeness, the basic aspects of the model, with special emphasis on sandy soils, are summarized in this section.

Any combination of three independent stress invariants is also an invariant. On the basis of a shifted stress, first and third stress invariants are defined as follows:

$$P = \frac{-1}{3} (\sigma_1 + \sigma_2 + \sigma_3) \quad (1)$$

$$L = - [(\sigma_1 - \sigma_s)(\sigma_2 - \sigma_s)(\sigma_3 - \sigma_s) + \sigma_s^3]^{1/3} \quad (2)$$

in which σ_1 , σ_2 , and σ_3 are principal components of stress, and σ_s is a parameter that can be defined as the cohesion. For physical reasons and also for the sake of numerical stability, σ_s is taken to be a small positive stress. On the basis of previous results (11), the limit surface (line) is assumed to satisfy the relation

$$L = \gamma_L P - \sigma_s \quad (3)$$

in which γ_L is obtained so that the limit line is an optimal fit to the data in a least-squares sense.

A flow function is chosen to be

$$\phi = \gamma P - L - \sigma_s - \sigma_a \quad (4)$$

in which γ is a strain-hardening function. The additional function, σ_a , depends only on strain rate and can be interpreted as an enhancement of cohesion based on rate effects. The theory falls within the general category considered by Rubin (9).

The flow surface $\phi = 0$ is also a line in the L-P space. As hardening occurs, γ decreases from an initial value of γ_0 to a limit value, γ_L . Softening is modeled by allowing γ to increase after the limit state. The general features of the model are shown in Fig. 1, which also illustrates how the presence of σ_a extends the elastic regime.

An appropriate function for γ is developed by assuming that a path-length inelastic-strain invariant, \bar{e}^i , exists and that it has a unique value, \bar{e}_L^i , at the limit state no matter which path is followed. One function that provides the initial value of $\gamma = \gamma_0$ when $\bar{e}^i = 0$ and the limit-state value of $\gamma = \gamma_L$ when $\bar{e}^i = \bar{e}_L^i$ is the following:

$$\gamma = \gamma_0 + (\gamma_L - \gamma_0) \sin \frac{\pi}{2} \left(\frac{\bar{e}^i}{\bar{e}_L^i} \right)^n \quad (5)$$

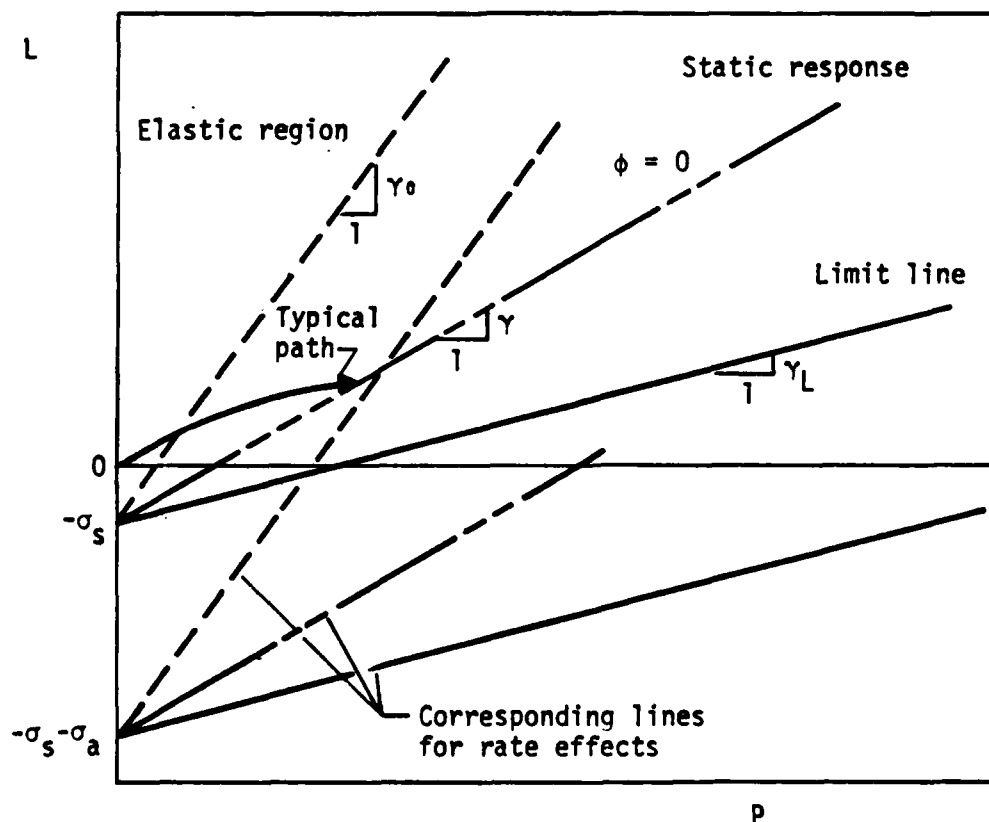


Figure 1. General features of viscoplastic model in L-P plane.

The parameter n can be chosen to provide theoretical curves that have the characteristic elastic-plastic shape of the experimental stress-strain curves, although detailed fits cannot be expected when merely a one-parameter function is used.

Because an associated flow rule provides too much dilatation, a potential function of the following form is used:

$$\phi^* = \gamma^* P - L - \sigma_s \quad (6)$$

where

$$\gamma^* = \gamma + b \quad (7)$$

and b is a material constant. A nonassociated flow rule implies that the inelastic strain increment is given by

$$\begin{aligned} d\mathbf{e}^i &= d\lambda \frac{\partial \phi^*}{\partial \mathbf{g}} \\ &= d\lambda \left(\frac{\partial \phi}{\partial \mathbf{g}} + b \frac{\partial P}{\partial \mathbf{g}} \right) \\ &= d\lambda \left(\frac{\partial \phi}{\partial \mathbf{g}} - \frac{b}{3} \mathbf{I} \right) \end{aligned} \quad (8)$$

in which \mathbf{g} and \mathbf{I} denote the stress and identity tensors, respectively, and $d\lambda$ is a positive parameter whose value is obtained by solving the consistency condition

$$\phi = 0 \quad (9)$$

Equation 8 shows that if b is positive, dilatation is reduced from that given by the associated flow rule. For hydrostatic compaction, and if σ_s is negligible with respect to P , L is approximately equal to P and the volumetric inelastic strain increment is given by

$$\begin{aligned} de_v^i &= \text{trace } de^i \\ &= d\lambda(1 - \gamma - b) \end{aligned} \quad (10)$$

The requirement that a hydrostatic loading path should always yield compaction is satisfied if $b > 1 - \gamma_L$. If only triaxial loading paths are available, b is chosen by trial and error to provide an optimal fit for the ensemble of paths.

For metal plasticity, \bar{e}^i is chosen to be the path length of the second invariant of the inelastic strain deviator. The use of the second invariant for soils is inappropriate because inelasticity occurs in soils subjected to hydrostatic loading. It has been found (12) that a weighted combination of first and third invariants is useful for defining a strain invariant for concrete. It is postulated that the same approach can be used for soils. Therefore, the differential of the path-length strain invariant is defined by

$$d\bar{e}^i = \frac{P_0}{P + P_0} (d\bar{e}_1^i + c d\bar{e}_3^i) \quad (11)$$

in which c and P_0 are material parameters, and

$$d\bar{e}_1^i = \left| \text{tr } de^i \right| \quad (12)$$

$$d\bar{e}_3^i = \left| \det (de^i) \right|^{1/3} \quad (13)$$

represent differentials of the absolute values for the first and third invariants, respectively. If P_0 is large, the effect of P is minimal. If P_0 is small, $\bar{\epsilon}^i$ accumulates less rapidly as P increases, a feature exhibited by many frictional materials. The parameter c controls the relative importance of the first and third invariants.

The use of the invariant $\bar{\epsilon}^i$ is useful only if $\bar{\epsilon}_L^i$ is the same for all possible paths. Inevitably, there will be scatter in the experimental value of $\bar{\epsilon}_L^i$ if data are available for a number of paths, but P_0 and c can be chosen to minimize the dispersion.

If linear isotropic elasticity is assumed, the specification of Young's modulus, E , and Poisson's ratio, ν , completes the model except for the rate effects. Because very few data involving strain rate are available, the following simple relation is assumed:

$$\sigma_a = \sigma_0 \left(\frac{\dot{\bar{\epsilon}}}{\dot{\bar{\epsilon}}_0} \right)^m \quad (14)$$

The total strain invariant, $\bar{\epsilon}$, is defined by using the same parameters as those used for $\bar{\epsilon}^i$ in Eq. 11. The parameters σ_0 and m are chosen to provide the general characteristics of enhancement as indicated by experimental data. The reference strain rate, $\dot{\bar{\epsilon}}_0$, is chosen merely to make the argument dimensionless for the exponential operation.

The model outlined in this section follows the concepts of classical plasticity; therefore, the development of an algorithm for incorporating the constitutive equation into computer codes presents no problem. The material

parameters E , ν , σ_s , γ_L , n , b , c , P_0 , σ_0 , and m represent a large but manageable set, especially in light of the wide range of response characteristics that can be predicted. In the next section material parameters and theoretical predictions are given for the response of two sands under both static and dynamic conditions.

COMPARISONS WITH EXPERIMENTAL DATA

Large strain-rate testing of soils presents many problems for the experimentalist. For example, if a specimen is loaded too rapidly, the propagation of stress waves will create nonuniform conditions of stress and strain in the sample. Whitman (13) points out that in the case of triaxial samples, the effect of lateral inertia must be included in a comprehensive assessment of failure and material properties. For specimens 4 inches long and 1.5 inches in diameter, he notes that the time to failure should be greater than 5 ms if lateral inertia is to be ignored.

In the case of dynamic uniaxial strain testing, the rate of loading is so rapid that no drainage occurs, particularly in fine-grained soils. Here thinner samples are typically used in order to prevent the formation of nonuniform conditions of stress and strain as well as to reduce side friction effects between the sample and equipment boundaries. However, Schindler (10) has developed equipment that can be used to test samples as large as 10 inches in diameter and 2-1/2 inches thick. The advantages of testing larger samples are reported to be (1) reduced disturbance at the boundaries, (2) increased magnitude of the displacements recorded and thereby improved accuracy of the measurements, and (3) measurement of displacement at several points on the sample face. It can be shown that if the rise-time of the loading pulse is long

relative to the time required for the propagating stress wave to traverse the distance back and forth between a rigid boundary and a free-surface boundary, then inertial stresses may be neglected. This principle, called the multiple reflection technique, has been the basis for the construction of many dynamic uniaxial strain test facilities.

The triaxial test apparatus used by Ito and Fujimoto (3), in which an hydraulic oil pump was employed, was reported to be capable of providing axial loads with variable displacement rates of from 0.04 mm/s to 600 mm/s. A load cell was used to measure axial loads and an eddy current type transducer to measure axial displacements. Radial displacements were recorded by six optical displacement transducers having a sensitivity of 0.01 mm. The average radial displacement was used in the volume change calculations. Air was used to apply the confining pressure. In order to reduce friction at the sample ends, two sheets of rubber lubricated with silicon grease were placed at each end of the sample, between the sample and the end-plate.

Two types of uniaxial strain test equipment were used by WES (4). The first was a 100-MPa gas-driven ram device, similar in concept to the apparatus described by Schindler (10). Capabilities include piston loads up to 450,000 N, rise-times as short as 3 ms, and decay times as short as 20 ms. The piston pressurizes an oil-filled chamber that produces the load on the sample face. Because of the high lateral stresses created in the sample, the device must be very rigid in order to prevent radial deformations from occurring. In the second device, recently developed by WES, an explosive charge drives the piston into the oil. Pressures up to 100 MPa may be obtained, with rise-times and decay times as short as 0.3 ms. The samples used in these devices are quite thin (1.27 cm) because of the previously mentioned requirement that the rise-time of the loading be long in relation to the transit time

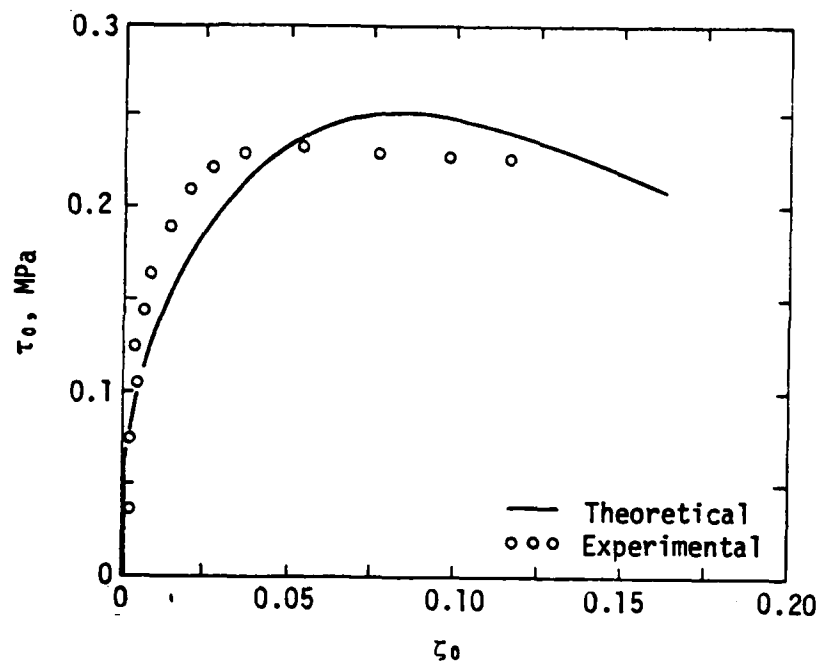
if the multiple reflection theory is to be valid. The sample height-to-diameter ratio was 1:76 in the WES tests.

For the data provided by Ito and Fujimoto (3), the model variables were adjusted to obtain an adequate fit to the static triaxial compression tests. The variables used were $E = 1300$ MPa, $\nu = 0.25$, $\bar{e}_L^i = 0.19$, $\sigma_s = 0.007$ MPa, $\gamma_0 = 1.06$, $\gamma_L = 0.86$, $n = 0.45$, $b = 0.33$, $c = 1.8$, $P_0 = -5$ MPa, $\sigma_0 = 0.19$ MPa, and $m = 0.75$. Two tests, conducted at different confining pressures (0.2 and 0.3 MPa), were available for defining parameters. The samples of Toyoura sand used in these tests were air-dried and had an initial void ratio of 0.72. The experimental results and theoretical predictions for the static tests are shown in Fig. 2 as plots of octahedral shear stress (τ_0) versus octahedral shear strain (ζ_0). In terms of principal stresses and strains, τ_0 and ζ_0 are given by

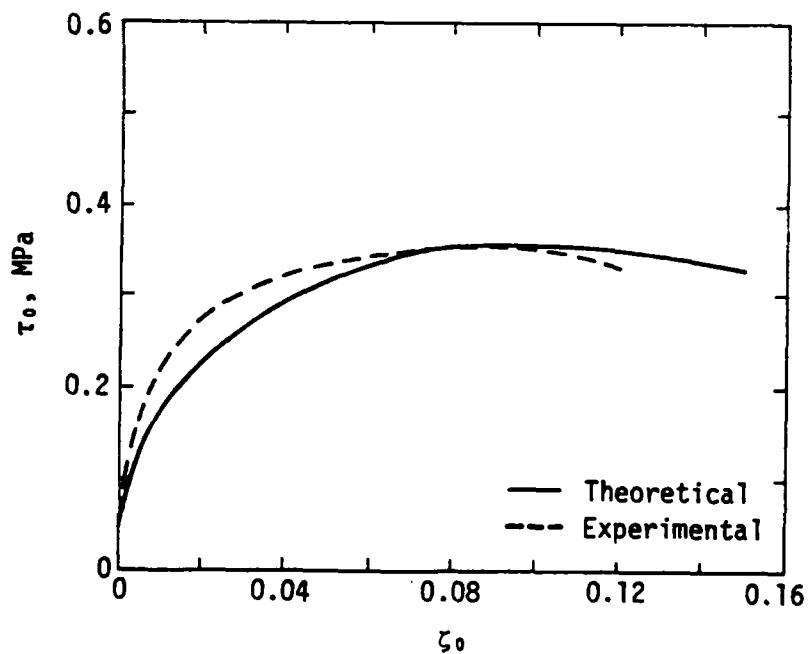
$$\tau_0 = \frac{1}{3} [(\sigma_1 - \sigma_2)^2 + (\sigma_2 - \sigma_3)^2 + (\sigma_3 - \sigma_1)^2]^{1/2} \quad (15)$$

$$\zeta_0 = \frac{1}{3} [(e_1 - e_2)^2 + (e_2 - e_3)^2 + (e_3 - e_1)^2]^{1/2} \quad (16)$$

Corresponding results are shown in Fig. 3 for the case in which the axial strain rate is 1/s. Both the theoretical and the experimental results show some enhancement of strength together with a shift in strain at the limit state. The model predicts a steeper response up to a higher level of stress for the rate-effect case than for the static case. This prediction is supported by experimental data when the confining pressure is 0.3 MPa but not when the confining pressure is 0.2 MPa. The reason for this discrepancy is not clear.

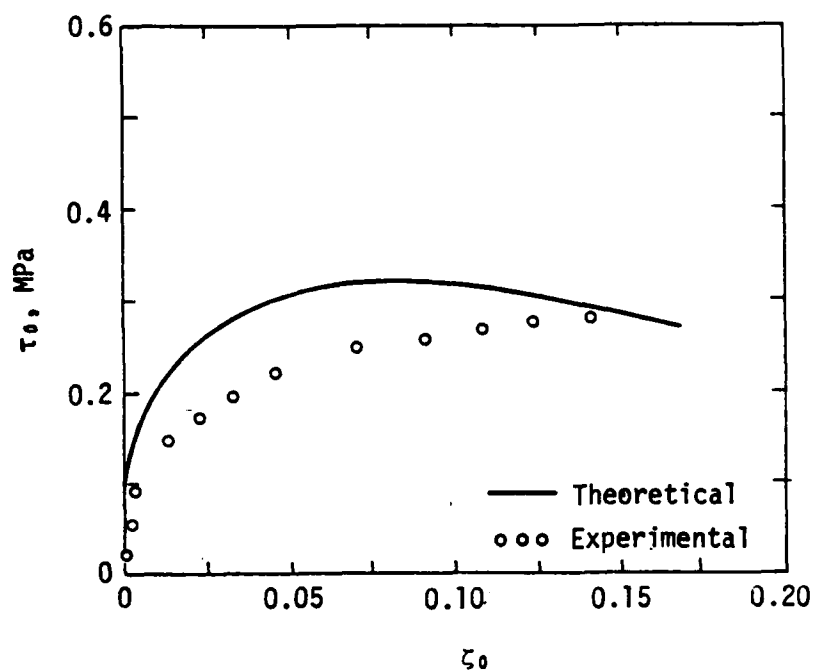


(a) Confining pressure 0.2 MPa.

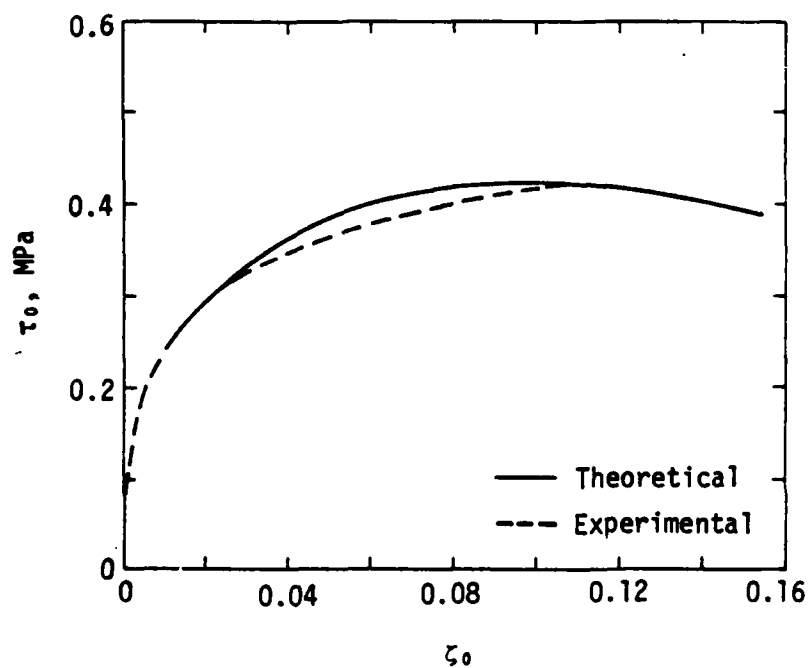


(b) Confining pressure 0.3 MPa

Figure 2. Theoretical and experimental (3) results for triaxial compression of sand.



(a) Confining pressure 0.2 MPa.



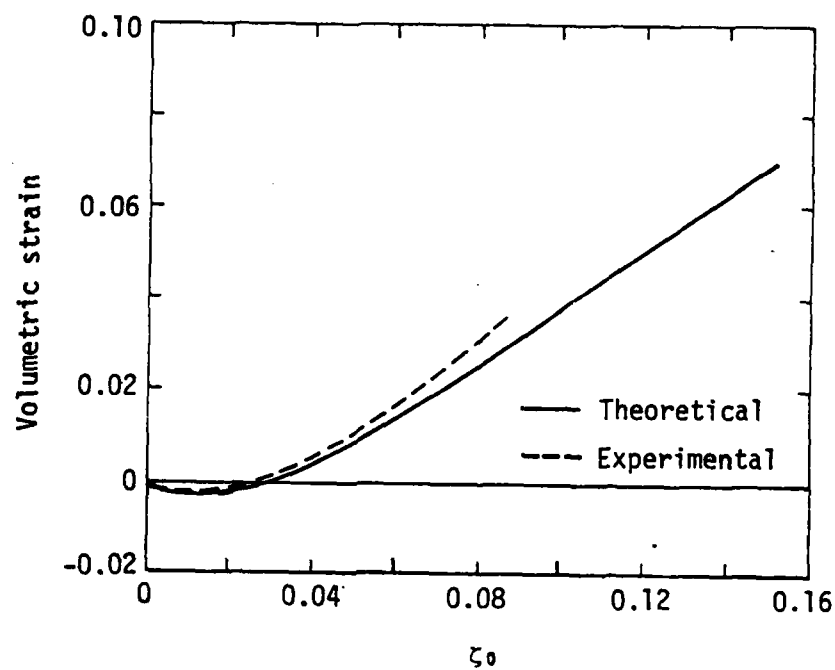
(b) Confining pressure 0.3 MPa.

Figure 3. Theoretical and experimental (3) results for triaxial compression of sand, longitudinal strain rate 1/s.

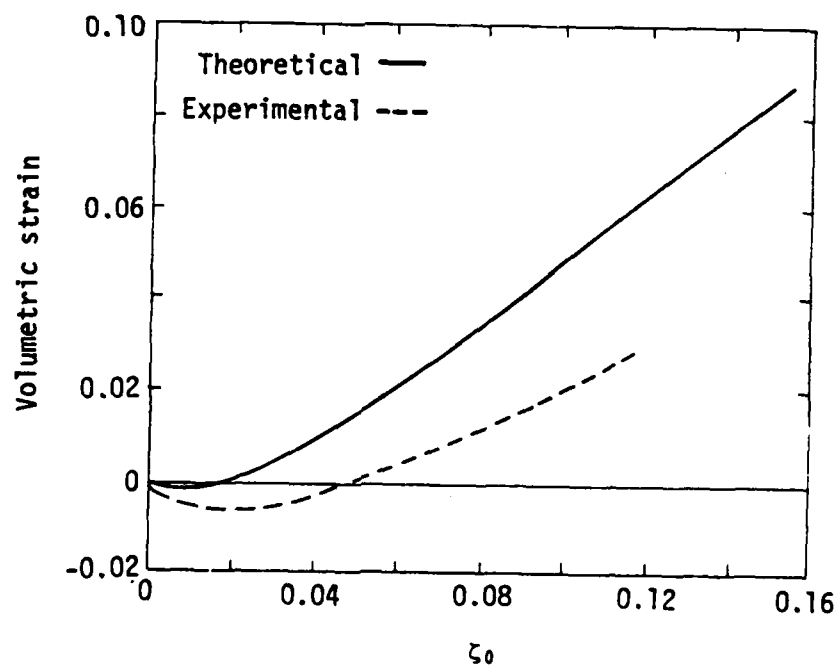
Volumetric strain as a function of octahedral strain for the triaxial path with a confining pressure of 0.3 MPa is shown for the static and dynamic cases in Figs. 4a and 4b, respectively. No volumetric data for a confining pressure of 0.2 MPa were presented in Ref. 3. Slightly more dilatation is predicted for the dynamic case than for the static case, but the experimental data show a significant reduction in dilatation. Whitman (13) indicates that more rather than less dilatation should be expected with higher rates of loading, but there is no experimental evidence to corroborate this statement.

The stress-strain results illustrated in Figs. 2 through 4 represent the response of sand subjected to relatively small confining pressures and strain rates. The WES data (4), on the other hand, represent the response of a clayey sand subjected to confining pressures higher by an order of magnitude and strain rates higher by two orders of magnitude than those imposed upon the sand. The representation of both loading situations by one model indicates that fundamental response features are contained within the constitutive relation.

The following parameters, chosen to fit the experimental data for the clayey sand, were used in the analysis of the WES data: $E = 1200$ MPa, $\nu = 0.25$, $\sigma_s = 0.1$ MPa, $\bar{e}_L^i = 0.55$, $\gamma_0 = 1.2$, $\gamma_L = 0.82$, $n = 0.4$, $b = 0.35$, $c = 3.2$, $P_0 = -32.5$ MPa, $\sigma_0 = 0.007$ MPa, and $m = 0.30$. The data consisted of stress and strain results for two static triaxial compression tests performed at confining pressures of 2.07 MPa and 4.14 MPa and for a uniaxial strain test during which lateral stress measurements were made. Figs. 5 and 6 compare the theoretical predictions with the experimental data. The agreement is considered excellent.

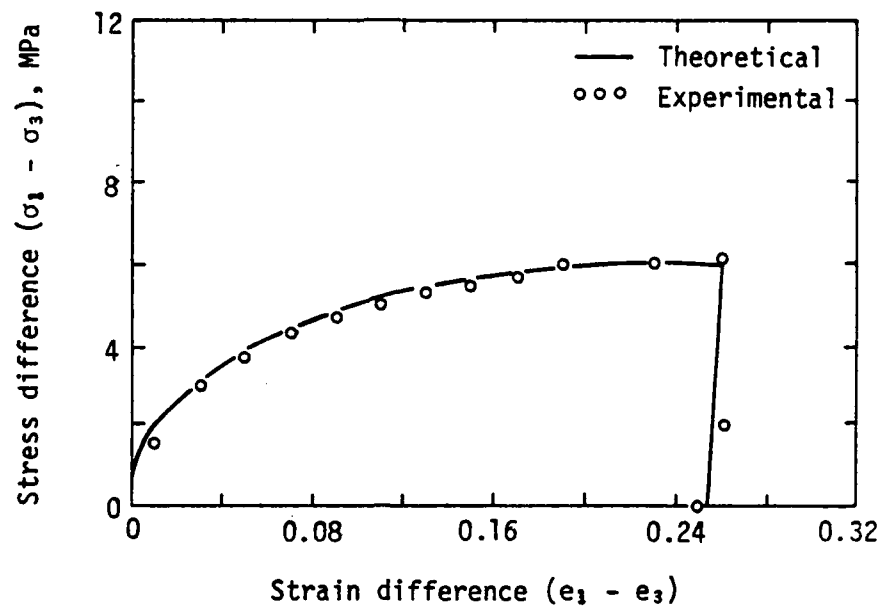


(a) Strain rate = 0.

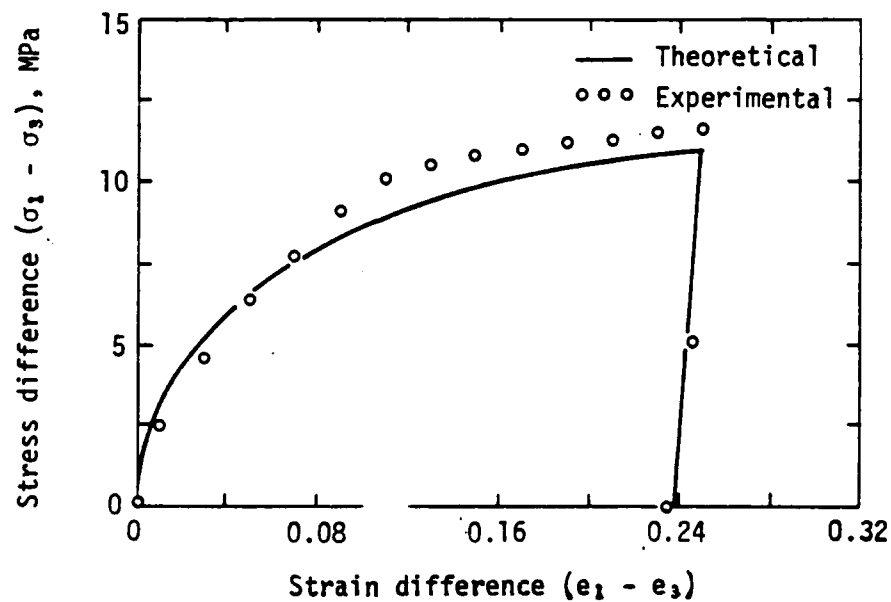


(b) Longitudinal strain rate = 1/s.

Figure 4. Theoretical and experimental (3) volumetric results for triaxial compression, confining pressure 0.3 MPa.

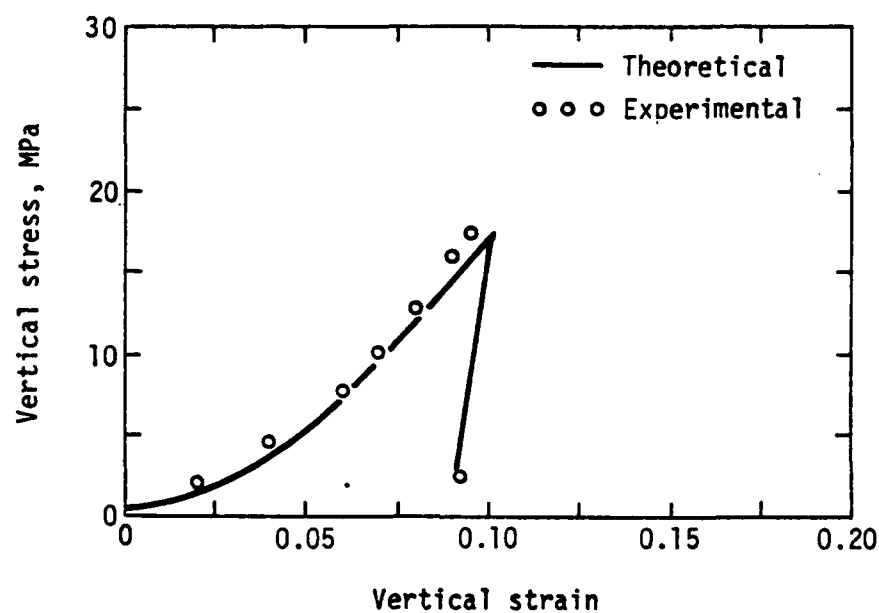


(a) Confining pressure 2.07 MPa.

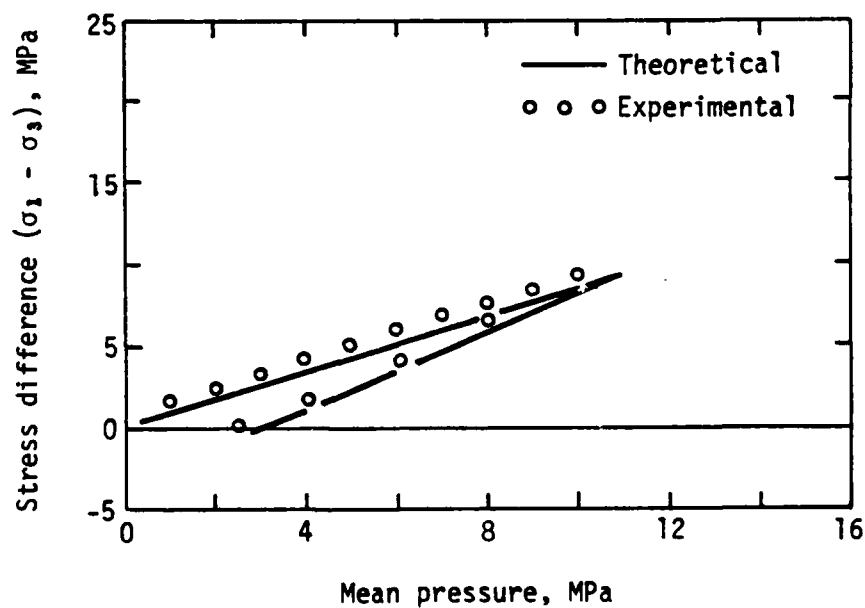


(b) Confining pressure 4.14 MPa.

Figure 5. Theoretical and experimental (4) results for triaxial compression of clayey sand.



(a) Vertical stress versus vertical strain.



(b) Stress difference versus mean pressure.

Figure 6. Theoretical and experimental (4) results for uniaxial strain.

The WES dynamic data were obtained from dynamic uniaxial strain tests, each of which was performed at varying strain rates. The strain histories for two cases (Fig. 7) were obtained by choosing strain and time values from plots of vertical stress versus time and vertical stress versus vertical strain presented in Ref. 4. The maximum uniaxial strain rate is approximately 200/s for both cases.

Spline fits to the experimental data (Fig. 7) were used as input to the model to obtain theoretical values of stress. Fig. 8 is a comparison of the theoretical predictions and experimental results for the dynamic uniaxial tests. The response of the soil is extremely different from that obtained in the static test. Here the vertical stress-vertical strain curve is convex to the strain axis, whereas the static test shows the more conventional response: concave toward the strain axis. The viscoplastic model has captured this feature at least qualitatively.

The softening response is due to a decrease in strain rate rather than to the actual strain-softening type of behavior that might be seen in static triaxial tests. Unfortunately, lateral stress measurements were not measured for the dynamic test, and no dynamic triaxial test results are available for this material.

CONCLUSIONS

The elasto-viscoplastic model presented here has been shown to be capable of predicting the stress-strain and volumetric strain response of soils (sand and clayey sand) to a selected group of tests (triaxial compression and uniaxial strain). The model has been used to predict soil response to strain rates as high as 200/s. The dramatic changes in soil behavior associated with rate

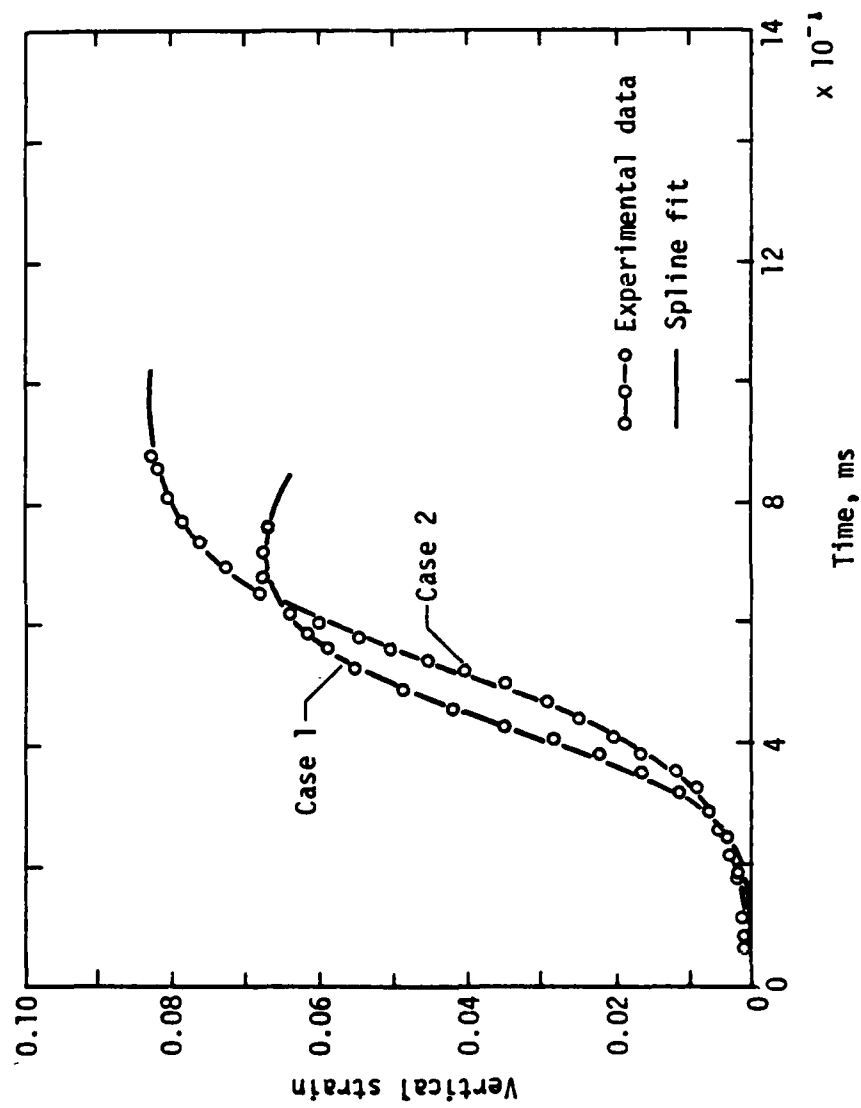
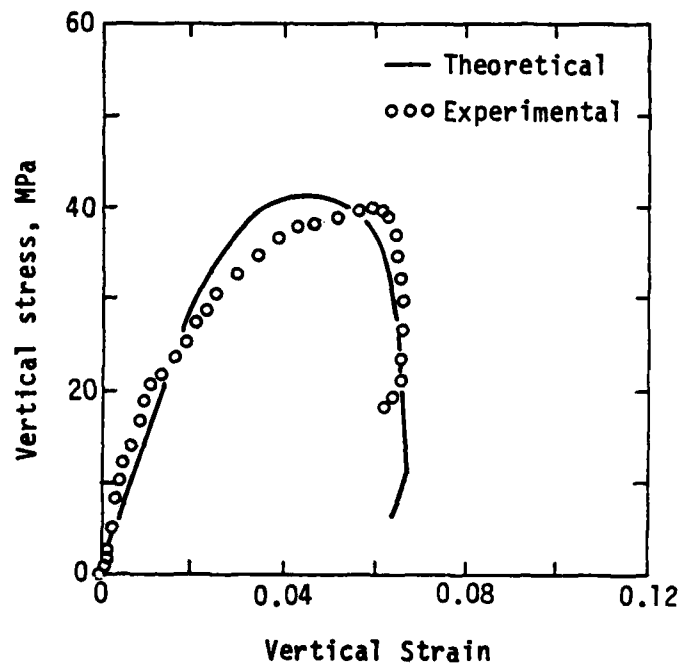
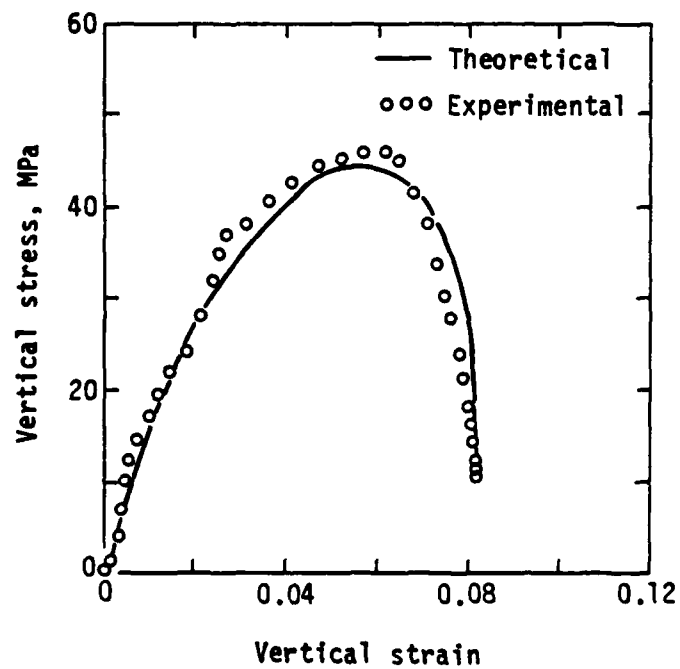


Figure 7. Vertical strain as a function of time for WES data.



(a) Case 1.



(b) Case 2.

Figure 8. Theoretical and experimental (4) results for high uniaxial strain rates.

effects are reproduced by the model. The combination of mathematical simplicity and realistic predictions make the model particularly appropriate for computer codes used to study soil response to dynamic loading.

ACKNOWLEDGMENTS

This research was supported by the Air Force Office of Scientific Research. D. Hayden performed many of the calculations from which theoretical data for the figures were obtained.

REFERENCES

1. Baladi, G. Y., and Rohani, B., "Development of an Elastic-Viscoplastic Constitutive Relationship for Earth Materials," Proceedings, International Conference on Constitutive Laws for Engineering Materials, Theory and Application, C. S. Desai and R. H. Gallagher, Eds., Tucson, Arizona, January 10-14, 1983, pp. 521-523.
2. Drucker, D. C., Gibson, R. E., and Henkel, D. J., "Soil Mechanics and Work-Hardening Theories of Plasticity," Transactions of the ASCE, 122, 1957, pp. 338-346.
3. Ito, T., and Fujimoto, K., "Strain Rate Effects on Stress-Strain Relationships of Sand," Proceedings of the 30th Japan National Conference for Applied Mechanics, Vol. 30, University of Tokyo Press, 1980, pp. 17-24.

4. Jackson, F. G., Ehrgott, J. Q., and Rohani, B., "Loading Rate Effects on Compressibility of Sand," Journal of the Geotechnical Engineering Division, ASCE, Vol. 106, No. GT8, August 1980, pp. 839-852.
5. Lade, P. V., "Elasto-Plastic Stress-Strain Theory for Cohesionless Soil with Curved Yield Surfaces," International Journal of Solids and Structures, Vol. 13, 1977, pp. 1019-1035.
6. Lade, P. V., and Duncan, J. M., "Cubical Triaxial Tests on Cohesionless Soil," Journal of the Soil Mechanics and Foundations Division, ASCE, Vol. 99, 1973, pp. 793-812.
7. Nelson, I., Baron, M. L., and Sandler, I., "Mathematical Models for Geological Materials for Wave-Propagation Studies," Chapt. 13, Shock Waves and the Mechanical Properties of Solids, Syracuse University Press, Syracuse, New York, 1971, pp. 289-351.
8. Perzyna, P., "Fundamental Problems in Viscoplasticity," Advances in Applied Mechanics, Vol. 9, Academic Press, New York, 1966.
9. Rubin, M. B., "A Thermoelastic-Viscoplastic Model with a Rate-Dependent Yield Strength," Journal of Applied Mechanics, Vol. 49, June 1982, pp. 305-311.
10. Schindler, L., "An Improved Facility for Testing Soils in One-Dimensional Compression," Proceedings, International Symposium on Wave Propagation and Dynamic Properties of Earth Materials, University of New Mexico, Albuquerque, New Mexico, August 23-25, 1967, pp. 847-860.

11. Schreyer, H. L., "A Third-Invariant Plasticity Theory for Frictional Materials," J. of Structural Mechanics, Vol. 11(2), 1983, pp. 177-196.
12. Schreyer, H. L., and Babcock, S. M., "A Third-Invariant Plasticity Theory for Low-Strength Concrete," submitted for publication in ASCE Journal of Engineering Mechanics.
13. Whitman, R. V., The Response of Soils to Dynamic Loading, Contract Report No. 3-26, U.S. Army Engineer Waterways Experiment Station, Corps of Engineers, Vicksburg, Mississippi, May 1970.

NOTATION

The following symbols are used in this paper:

- b = material parameter;
- c_2 = material parameter;
- $d\lambda$ = path-length parameter;
- E = Young's modulus;
- e_1, e_2, e_3 = principal strains;
- e_v^i = inelastic volumetric strain;
- \bar{e} = total strain invariant;
- \bar{e}^i = path-length inelastic-strain invariant;
- \bar{e}_L^i = path-length strain-invariant limit value;
- $\bar{\epsilon}_0$ = reference strain rate;
- \mathbf{e}^i = inelastic strain tensor;
- \mathbf{I} = identity tensor;
- L = stress invariant;

m = material parameter;
 n = material parameter;
 P = mean pressure;
 P_0 = material parameter with units of pressure;
 γ = slope of flow surface in L-P space;
 γ_L = slope of limit surface in L-P space;
 γ_0 = initial slope of flow surface in L-P space;
 γ^* = slope of potential surface in L-P space;
 τ_0 = octahedral shear strain;
 ν = Poisson's ratio;
 σ_a = additional cohesion due to strain rate;
 σ_s = cohesion;
 σ_0 = material parameter;
 $\sigma_1, \sigma_2, \sigma_3$ = principal stresses;
 $\underline{\sigma}$ = stress tensor;
 τ_0 = octahedral shear stress;
 ϕ = flow function; and
 ϕ^* = potential function.

END

FILMED

6-11-68

DTIC